Recent Progress on Dominant Sulfide-type Solid-state Na Superionic Conductors for Solid-state Sodium Batteries

Xiaolin Guo, Selim Halacoglu, Yan Chen, Hui Wang*

X. Guo, S. Halacoglu, Prof. H. Wang,
Mechanical Engineering Department, University of Louisville, 40292, USA
E-mail: hui.wang.1@louisville.edu

Dr. Y. Chen
Neutron Scattering Division, Oak Ridge National Laboratory, 37830, USA

Keywords: Sodium, Solid-State, Ion-Conductors, Sulfide, Structure

Abstract

Over the past decade, solid-state batteries have garnered significant attentions due to their potentials to deliver high energy density and excellent safety as a promising next-generation energy storage system. Considering the abundant sodium (Na) resources in contrast to lithium (Li), the development of sodium-based batteries has become increasingly appealing. As a key component in solid-state Na batteries, sulfide-based superionic conductors are widely considered as promising and under intensive investigation due to the features of high ionic conductivity and cold-press densification capability. In recent years, tremendous efforts have been made to investigate sulfide-based Na-ion conductors on their synthesis, compositions, conductivity, and the feasibility in solid-state Na batteries. However, there are still several challenges to overcome for them to realize high performance solid-state Na batteries. This article provides a comprehensive update on the synthesis, structure, and properties of three dominant sulfide-based Na-ion conductors (Na_3PS_4, Na_3SbS_4, and $Na_{11}Sn_2PS_{12}$), and their families that have a variety of anion and cation doping for structure modifications and property optimizations. Additionally, we reviewed the interface stability of these sulfide electrolytes towards the anode, as well as the electrochemical cycling performance solid-state Na batteries based on different types of cathode materials (metal sulfides, oxides and organic cathodes). Finally, we discuss the perspective and outlook for the development and practical utilization of sulfide-based Na-ion conductors in solid-state batteries.

1. Introduction

Solid-state alkali metal batteries that utilize solid ion-conductors to replace organic liquid electrolytes have gained tremendous research interests in the past decade due to the potential advantages of high energy density and enhanced safety.[1-4] By using solid electrolytes, it enables more advanced designs such as bipolar stacked batteries instead of single cells, thus boosts the volume energy density and facilitates for the integration of such batteries into power systems. Compared to lithium-ion batteries (LIBs) and Li metal batteries, rechargeable sodium (Na) batteries have attracted serious attention for large scale energy storage systems due to the appropriate electrochemical voltage windows (-2.7 V compared to -3.04 V for Li *vs.* standard hydrogen electrode) and more abundant resources of Na than Li in the Earth's crust.[5-8] Thus, in parallel to the intense development of Li-ion conductors, there is also a rising interest on Na-ion conductors as solid electrolytes for solid-state Na batteries.

In the structure of a solid-state battery, the solid electrolytes (SE) play the dual roles of (i) electronically insulate and physically blocking and (ii) transporting ions between the anode and cathode. To fulfill the main needs, the ideal SEs are expected to hold the following features:[8-10] high ionic conductivity at room temperature (RT) while negligible electronic conductivity; great structure and chemical stability; wide electrochemical window and good compatibility with electrodes (anode and cathode); robust mechanical properties, simple and scalable synthetic approaches, etc. The popular Na-ion conductive materials can be classified into inorganic, polymers, and composites.[6, 7, 11] The state-of-art inorganic Na-ion conductors are classified into four categories: oxides (e.g. β-Al_2O_3 and NASICON-type conductors),[12-15] sulfides (e.g. Na_3PS_4, Na_3SbS_4),[16-18] halides (e.g. Na_2ZrCl_6),[19, 20] and hydrides (e.g. $NaBH_4$).[21, 22] So far, oxide SEs such as β-Al_2O_3 have been successfully commercialized in Na-S batteries and ZEBRA batteries.[12, 23, 24]

Compared with oxides, sulfide-based conductors generally have higher ionic conductivity and require mild synthesis and processing temperatures, although they have their own issues such as air and moisture sensitivity.[17, 25, 26] Sulfide-based solid conductors normally can achieve high density and great ionic conductivity via cold-pressing at RT, other than high temperature sintering for most oxide conductors. Moreover, a more "soft" sulfides would be favorable to accommodate the volume changes for the intercalation and deintercalation of Na ions during the battery cycling.[27] There have been several important review articles for solid electrolytes in LIBs or Li metal batteries.[28-34] Nevertheless, the review articles on sulfide SEs are mainly focus on Li-ion conductors and slightly mention Na-ion conductors.[25, 26] On the other hand, there have been tremendous efforts devoted to sulfide and chalcogenide Na-ion conductors in the past decade. Thus, a comprehensive review article to update the important progress and development in this field is timely and necessary.

Sulfide-type Na-ion conductors start to attract serious attention after the inspiring report on superionic Na_3PS_4 glass-ceramic with impressive ionic conductivity.[35] Later, research efforts also expand to Na_3SbS_4 with the replacement of P by Sb element, and a new sulfide compound $Na_{11}SnP_2S_{12}$ from both theoretical and experimental works. Besides, other sulfides-based Na-ion conductors such as Na_4MS_4 (M=Sn, Si, Group IVA elements) have been studied. In comparation with Na_4SnS_4, $Na_4Sn_{0.67}Si_{0.33}S_4$ with Si doping shows a new space group $I4_1/acd$ and 3D diffusion pathway, yielding to a higher ionic conductivity of 1.6 mS cm^{-1}.[36] Recently, research on sulfide-type conductors with Groups IIIA elements (e.g., B, Ga) have been reported. For example, Na_3BS_3 that containing boron as a electrochemically inert element to form an insulating thin interlayer toward Na,[37] and $Na_3B_5S_9$ as a new thioborate contains supertetrahedral clusters to create 3D diffusion channels housing Na-ions.[38] Among those recent discoveries, Na_3PS_4, Na_3SbS_4, and $Na_{11}Sn_2PS_{12}$ compounds are considered as the most widely studied sulfide-based Na-ion conductors.

In this review article, we focus on these three (Na_3PS_4, Na_3SbS_4, and $Na_{11}Sn_2PS_{12}$) dominant sulfide-type Na-ion conductors to report their recent progress and most exciting developments. First, we introduce four different synthesis approaches for sulfide-type conductors, and then discuss the doping chemistry effects on the crystal structure and Na-ion conduction mechanisms as well as conductive properties. Later, we review the recent studies of interface stability between sulfide SEs toward Na anode and the efforts on interface modification strategies. Moreover, we report the composite cathode design and the electrochemical cycling performance of sulfide SEs in solid-state Na batteries. Finally, a brief perspective is provided for future research on sulfide-type Na-ion conductors for solid-state batteries. **Figure 1** displays the timeline summary of these sulfide-type SEs with important conductivity and doping chemistry from the experimental sides. This review analyzes the sulfide Na-ion conductors from material synthesis approach, fundamental doping chemistry, ion transport mechanism, interface stability and cathode design. The aim is to encourage more research on discovering novel SE materials and advancing their applications in solid-state Na batteries.

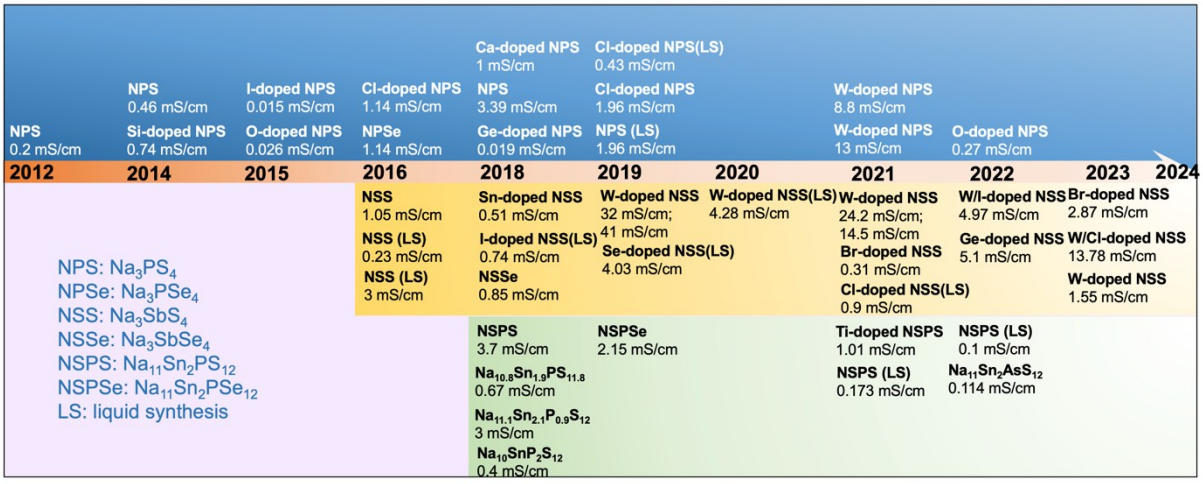

Figure 1. Timeline summary of the representative sulfide-based Na-ion conductors (Na_3PS_4, Na_3SbS_4, and $Na_{11}Sn_2PS_{12}$) with the important ionic conductivity and doping chemistry from experiments. (if not marked on LS, the SE is from solid state approach) Refs. (NPS/Se-based SEs: refs.[16, 39-50]; NSS/Se-based SEs:[18, 49, 51-57]; NSPS/Se SEs:[58-63])

2. Synthesis Methods

The commonly used preparation methods for sulfide-based Na-ion conductors can be classified into *solid-state approach* and *wet-chemical approach* (**Figure 2**). Solid-state approach includes (i) mechanochemical synthesis and (ii) solid-state reaction depending on the ball milling and heat treatment conditions, while wet-chemical synthesis involves (i) organic solvent-based approach and (ii) aqueous-based method that dependent on the solvent categories. **Table 1** presents a comparison of the advantages and challenges associated with each individual method. There are additional synthetic approaches such as direct decomposition[64], which are not detailed here.

2.1. Solid-state Approach

In a typical solid-state approach, the precursors are dry mixed (and/or mechanical ball milled) and subsequently heated to a temperature in the range of 260-700 ºC, depending on the reaction thermodynamics. During the process, the ball milling parameters (energy, frequency and time), and the heat treatment parameters (such as temperature, dwell time, heating rate and cooling rate) can be adjusted to control the crystal structure of the products that is favorable for ion conduction. Depending on the ball milling conditions and heat treatment temperatures, the solid-state approach is divided into (1) the mechanochemical method and (2) solid-state sintering reaction.

2.1.1. Mechanochemical method

In a mechanochemical method, the chemicals precursors (e.g. Na_2S and P_2S_5 for Na_3PS_4) with a stoichiometric ratio must be mechanically ball-milled for extended hours, and then subject heat treatment at mild temperatures (260~500 ºC) for different dwell time (several minutes to hours).[16, 26, 49] During the ball-milling process, the chemical reactions are driven by the mechanical force (mechanochemistry), and the energy input is in the form of mechanical impact. Thus, the ball milling step can lead to fine particle size and introduce defects, thus strongly influence the phase formation, crystal structure, microstructure, conductivity as well as the residual strain and stress in the yielded products.[65, 66] In addition, the ball milling

conditions also influence the Na-ion conductivity because (a) the micro- and macro-strains on the local and average scales influence the Na^+ diffusion and (b) highly efficient interparticle contact to enhance the surface conduction. The mechanochemical method has been demonstrated to synthesize all three types of sulfide SEs, including Na_3PS_4,[67-69] doped Na_3PS_4 ,[45, 70] doped-Na_3SbS_4,[49] and $Na_{10+x}Sn_{1+x}P_{2-x}S_{12}$.[71]

In 2016, Wagemaker et al. systematically restudied the ball milling conditions and annealing temperatures on the crystal structure and ionic conductivity of Na_3PS_4.[68] Under a low-speed ball milling (400 rpm), the diffraction peaks were observed after 5 hours and became more pronounced after 10 hours, with the peaks being indexed to cubic Na_3PS_4 (**Figure 3a**). Further, it was found that cubic Na_3PS_4 remained stable up to 250 °C while annealing above 300 °C resulted in a cubic-to-tetragonal phase transition. Meanwhile, the RT ionic conductivity of Na_3PS_4 decreased accompanying the phase transition. After annealing at 250 °C, cubic Na_3PS_4 exhibited the RT conductivity of 0.105 mS cm^{-1}; in contrast, the tetragonal Na_3PS_4 showed a lower ionic conductivity of 0.045 mS cm^{-1} after annealing at 450 °C. In the mechanochemical synthesis, the ball milling and annealing temperatures also influence the grain size and residual strain.[65] In specific, higher annealing temperature (500 °C) results in the larger grain size (200 nm) and strain release (0.1 %) than the lower temperature heat treatment (260 °C, 25 nm grain size, stain of 0.25%). Under a higher speed (550 rpm) of ball milling, Meng et al. reported that the Na_3PS_4 diffraction peaks were observed as early as after 10 minutes of ball milling.[69] More interestingly, the as-milled Na_3PS_4 (after one hour ball milling for phase formation) can achieve an impressive ionic conductivity of 0.17 mS cm^{-1} without heat treatment (**Figure 3b)**.

In addition to pure Na_3PS_4, the mechanochemical method also has been used to synthesize doped-Na_3PS_4 SEs with various cation or anion dopants such as Si, Ge, W, Se, O, etc.[40, 43, 45, 50, 70] and doped-Na_3SbS_4 SEs (W and Ge).[49, 72] Taking $Na_{3-x}P_{1-x}W_xS_4$ as an example, WS_2 was added to Na_2S, P_2S_5 and S as an additional chemical precursor for W doping. The mixture was

subjected to extended ball milling and heat treatment at different temperatures (220, 550 °C).[70] They reported the observation of $Na_{2.85}P_{0.85}W_{0.15}S_4$ phase in only the ball-milled sample, and the subsequent annealing process increased the phase crystallinity. However, after heat treatment at 550°C for 20 h without ball-milling, the impurity phase (WS_2) appeared. For the mechanochemical synthesis, the ionic conductivity is dependent on both doping content ($0<x<0.24$) and the subsequent heat treatment temperatures. The $Na_{2.85}P_{0.85}W_{0.15}S_4$ (ball-milled plus 550 °C heat treatment) achieved the highest ionic conductivity of 8.8 mS cm^{-1} at RT although it is still slightly lower than the solid-state method synthesis (13 mS cm^{-1}). Similarly, Hayashi and co-workers also reported the synthesis of W-doped Na_3SbS_4 using the mechanochemical method by the replacement of P_2S_5 by Sb_2S_3 in precursors.[49] After ball milling and annealing at 275 °C for crystallization, they obtained cubic phase $Na_{2.88}Sb_{0.88}W_{0.12}S_4$ solid electrolyte with the highest RT ionic conductivity of 32 mS cm^{-1}. Moreover, dual doping of anion/cation (W/I) is also attempted by the ball milling for 20 hours and heat treatment at 380 °C to achieve a high ionic conductivity of 4.9 mS cm^{-1} for Na_3SbS_4-$Na_2W_{0.77}S_4I_{0.6}$ SE.[73]

The mechanochemical process also has been employed for the synthesis of $Na_{11}Sn_2PnS_{12}$ (Pn=P, Sb) SEs.[74, 75] For the $Na_{11}Sn_2PS_{12}$ samples, the heat treatment temperatures of ball-milled samples on the optimization of the structure and conductivity were studied.[74] In this work, the pure phase $Na_{11}Sn_2PS_{12}$ was obtained after annealing at 260 or 300 °C, while higher temperatures (>400 °C) resulted in the formation of a secondary phase of Na_3PS_4. However, with the presence of Na_3PS_4 as the secondary phase, the 400 °C-treated sample showed the highest ionic conductivity of 0.3 mS cm^{-1} at RT, in comparison to 0.11 mS cm^{-1} for the sample after 300 °C heat treatment. In addition, Yao et al. reported using Sb to substitute P and partial replacement of Se to S to prepare $Na_{11}Sn_2SbS_{12-x}Se_x$ ($0<x<0.75$) sulfides.[75] By tuning the Se

content, they found that $Na_{11}Sn_2SbS_{11.5}Se_{0.5}$ reached the highest ionic conductivity of 0.66 mS cm^{-1} at RT.

2.1.2. High temperature solid-state synthesis

For a typical high temperature solid-state synthesis (**Figure 2b**), the chemical precursors are mixed (hand mixed or ball milled) and sealed in a quartz tube, then heated to a high temperature (≥550 °C) for annealing for an extended time (several hours to days), followed by cooling down (natural cooling or at a controlled cooling rate). This approach has been employed to synthesize Na_3PS_4, Na_3SbS_4 and doped Na_3SbS_4, as well as $Na_{11}Sn_2PS_{12}$ type SEs.

In general, the solid-state reactions after high temperature sintering yield to sulfides with the highest crystallinity and ionic conductivity. For example, the solid-state synthesized $Na_{2.85}P_{0.85}W_{0.15}S_4$ SE showed a higher RT ionic conductivity of 13 mS cm^{-1} higher than that of the sample from mechanochemical method (8.8 mS cm^{-1}).[70] In addition, Kanno et al. reported to use solid-state synthesis method to produce tetragonal Na_3PS_4 by heating the precursors (Na_2S and P_2S_5) to a high temperature sintering (700 °C), followed by quenching and further annealing (450 °C).[46]. With the high sintering temperature, the tetragonal Na_3PS_4 achieved the highest ionic conductivity of 3.39 mS cm^{-1} at 25 °C and the low activation energy (16.6 kJ mol^{-1}). This value is much higher than the previously reported of tetragonal Na_3PS_4 (0.05 mS cm^{-1})[16]. The dramatically increased conductivity is attributed to the introduced Na vacancies and expanded lattice volume through the optimized synthetic approach (ball milling, sintering, quenching, annealing). For Na_3SbS_4 SE, after heat treatment and melted at 700 °C, different post-treatment parameters such as ball milling energy and cooling rate were controlled to study the influence of these synthetic conditions on the structure and conductivity of produced Na_3SbS_4.[76] They observed that the high energy ball milling approach is the only way to obtain cubic-dominate phase, which shows an ionic conductivity of 2.8 mS cm^{-1}.

The high temperature sintering also helps to use individual elements as precursors to synthesize Na_3PnCh_4 (Pn=P, Sb, Ch=S, Se).[77-79] For example, Zhang et al. reported heating the mixture of Na metal, Sb, and S with stoichiometric proportion to 700 °C in a vacuum-sealed quartz tube and annealing for 12 hours to produce Na_3SbS_4 with the ionic conductivity of 3 mS cm^{-1}.[51] Similarly, $Na_3SbS_xSe_{4-x}$ ($0 \leq x \leq 4$) conductors were synthesized through a calcination process of the mixture of Na metal, Sb metal, S and/or Se powders in a sealed quartz tube at 650 °C for 18 hours.[79] When using Na, Sb, P and Se powders as chemical precursors, $Na_3P_{1-x}Sb_xSe_4$ SEs were obtained after heat treatment at 700 °C.[78]

High-temperature solid-state reactions are also employed to efficiently introduce various types of dopants (Ca, Sn, W, and I) into Na_3PS_4 or Na_3SbS_4,[44, 57, 80-82] resulting in either new crystalline structure and/or higher ionic conductivity. Beside pure Na_3PS_4, high temperature solid-state reaction is also employed to synthesize to $Na_{3-2x}Ca_xPS_4$ ($0 \leq x \leq 0.375$).[44] After heating at 700 °C for 24-48 hours, they obtained cubic $Na_{2.73}Ca_{0.135}PS_4$ (x=0.135) to achieve the maximum RT conductivity of 1 mS cm^{-1} due to the Na vacancies. In the other work, tetragonal $Na_{4-x}Sn_{1-x}Sb_xS_4$ ($0.02 \leq x \leq 0.33$) with space group $I4_1/acd$ was obtained by heating Na_2S, SnS_2, Sb_2S_3, and S at 550 °C for 12 hours.[80] In addition, W-doped Na_3PnS_4 (Pn=Sb, P) was also synthesized after a heat treatment at 550 °C for 20 hours in the other work.[81] With doping content x=0.1, $Na_{2.9}W_{0.1}Sb_{0.9}S_4$ and $Na_{2.9}W_{0.1}P_{0.9}S_4$ conductors exhibit very high values of RT ionic conductivity at 41 ± 8 mS cm^{-1} and 13 ± 3 mS cm^{-1}, respectively. When the W-doping content is high (x=0.3), the synthesized $Na_{2.7}W_{0.3}Sb_{0.7}S_4$ showed a new orthorhombic crystal structure and retained a high ionic conductivity of 14.5 mS cm^{-1}.[57]

The solid-state reaction approach is also used to produce quaternary system Na-Sn-Pn-Ch type sulfides (Pn=P, Sb, Ch=S, Se).[58, 61, 62, 83, 84] In 2018, Nazar et al. reported a tetragonal structured $Na_{11}Sn_2PS_{12}$ synthesized at 700 °C through the precursors of Na_2S, P_2S_5 and SnS_2. It exhibited an ionic conductivity of 1.4 mS cm^{-1} at RT and activation energy of 0.25 eV.[58] When using

Na_3PS_4 and Na_4SnS_4 as chemical precursors and annealing temperature of 600 °C, $Na_{11}Sn_2PS_{12}$ with even higher ionic conductivity of 3.7 mS cm^{-1} was obtained.[83] Moreover, Wang et al. also reported the synthesis of $Na_{10.8}Sn_{1.9}PS_{11.8}$ superionic conductor by adjusting the precursor materials (Na_2S, P, Sn and S), heat treatment (700 °C for 48 hours) and slow cooling rate.[62] Moreover, they also employed the precursors of Na_2Se, P, Sn and Se at a higher temperature (900 °C for 48 hours) to obtain $Na_{11}Sn_2PSe_{12}$ with a total ionic conductivity of 2.15 mS cm^{-1} at 25 °C.[61] Using Sb to partially substitute P, a series of $Na_{11+x}Sn_{2+x}(Sb_{1-y}P_y)_{1-x}S_{12}$ samples were synthesized by heating a sociochemical ratio of Na_2S, P_2S_5, SnS_2, Sb_2S_3, and S to complete the soli-state reactions at 650 °C for 12 hours.[84]

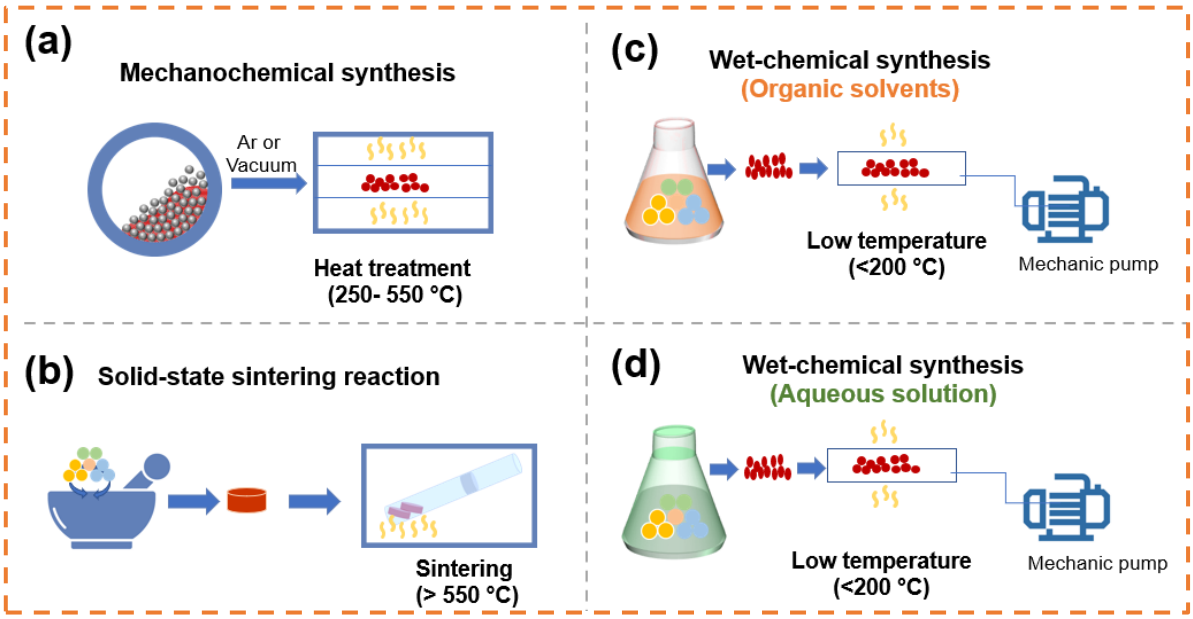

Figure 2. Scheme of different synthetic methods for sulfide-based Na-ion conductors: (a) Mechanochemical synthesis; (b) high temperature solid-state reaction; (c) wet-chemical synthesis using organic solvents; (d) wet-chemical synthesis using aqueous solution. The organic solvents include: NMF: *N*-methylformamide; DME:1,2-dimethoxyethane; DE: diethyl ether; MA: methyl acetate; ACN: acetonitrile; EDA: 1, 2-ethylenediamine; EDT: 1, 2-ethanedithiol.

Table 1. Comparison of Different Synthetic Approaches for Sulfide Na-ion Conductors

Methods		Advantages	Problems
Solid-state Approach	**Mechanochemical method**	Simple and straightforward	Often requiring subsequent heat treatment
	High temperature solid-state synthesis	High crystalline and phase purity	Requiring high temperature >500 °C under inert or protective environment
Wet-Chemical Approach	**Solvent-based synthesis**	Feasible and scalable	Products containing possible solvent residual that may decrease conductivity
	Aqueous-solution synthesis	Low-cost and non-toxicity	Not feasible for many conductors or precursors that are sensitive to water

2.2. Wet Chemical Synthesis

Different from the solid-state approach, the solvents are involved in the wet-chemical synthesis method (also named as liquid-synthesized) as a medium for the precursors mixing. After the mixing step, the solvents are removed by vacuum filtration or precipitation, and subsequent heat treatment at relatively low temperatures (**Figure 2c and d**). The wet-chemical synthesis method has several advantages,[52, 85-87] including (1) nanosized solid electrolyte particles; (2) the scalability for large-batch preparation and low temperatures heating and (3) the feasibility of forming an electrolyte coating on electrode particles to enhance the electrochemical performance. Previously, wet-chemical (or liquid-based) synthesis method is divided into suspension-based and solution-based.[86, 88] In this work, we describe the wet-chemical synthesis by their solvent categories: organic solvent-based and aqueous (water)-based.

2.2.1. Organic Solvent-based Synthesis

For pure Na_3PS_4, its wet-chemical synthesis method was attempted since 2015 by using N-Methylformamide (NMF) as the liquid solvent.[89] The produced cubic Na_3PS_4 (**Figure 3c**) contained impurity phases such as Na_3POS_3, thus leading to a poor ionic conductivity of 2.6 $\times 10^{-6}$ S cm^{-1} at RT, compared to the mechanochemical synthesized Na_3PS_4 (2.5×10^{-4} S cm^{-1}).[16] After that, various types of organic solvents have been explored to increase the phase purity and improve the RT ionic conductivity of liquid-synthesized Na_3PS_4 SEs.[48, 88, 90] When using

ether-based solvents such as 1,2-dimethoxyethane (DME) and diethyl ether (DEE),[90] the ionic conductivity of Na_3PS_4 increased to 1.8~2.6 $\times 10^{-5}$ S cm^{-1} at RT. Later, Hayashi et al. reported the synthesis of Na_3PS_4 by using DME solvent and subsequent heat treatment at different temperatures (270-480 °C).[88] With increasing temperatures, the ionic conductivity continuously increases until 0.26 mS cm^{-1} for the sample at 400 °C (NPS-400). Higher temperatures also resulted in larger particles in NPS-400 than in NPS-270 (**Figure 3d**). Besides, the Cl-doping further improved the liquid-synthesized $Na_{2.9375}PS_{3.9375}Cl_{0.0625}$ to achieve a high ionic conductivity of 0.43 $mScm^{-1}$ at RT.[88]

For wet-chemical synthesized pure Na_3SbS_4 and doped conductors, different types of solvents have been reported, such as ethanol, acetonitrile (ACN), etc.[53, 91-93] Wolden et al. compared the crystal structure of Na_3SbS_4 SEs that synthesized by using ethanol and water as solvents and dried at 140 °C.[91] The ethanol-produced Na_3SbS_4 exhibited broader XRD diffraction peaks, smaller crystallite size and higher ionic conductivity (0.52 mS cm^{-1}) compared to the sample that using water as the solvent (0.33 mS cm^{-1}). For Se-doped Na_3SbS_4 SEs, Yao et al. mixed Na_2S, Sb_2S_3, S and/or Se in ACN solvent and dried at 80 °C, followed by the heat treatment at 450 °C to obtain a series of $Na_3SbS_{4-x}Se_x$ ($0 \leq x \leq 0.75$) conductors.[93] Among them, tetragonal $Na_3SbS_{3.75}Se_{0.25}$ from the liquid-solid fusion method exhibited fine particle size and highest RT ionic conductivity of 4.03 mS cm^{-1}.

The wet-chemical method is also demonstrated to synthesize $Na_{11}Sn_2PS_{12}$ SE by mixing the precursors of Na_2S, P_2S_5, SnS_2 in DME solvent.[59] The liquid-synthesized $Na_{11}Sn_2PS_{12}$ showed a fine particle size of 200 nm, smaller than the sample from ball milling (**Figure 3e**). By the optimization of heat treatment temperatures (400~460 °C) for crystallization, the nanosized $Na_{11}Sn_2PS_{12}$ achieved the highest ionic conductivity of 0.173 S cm^{-1} at 25 °C.

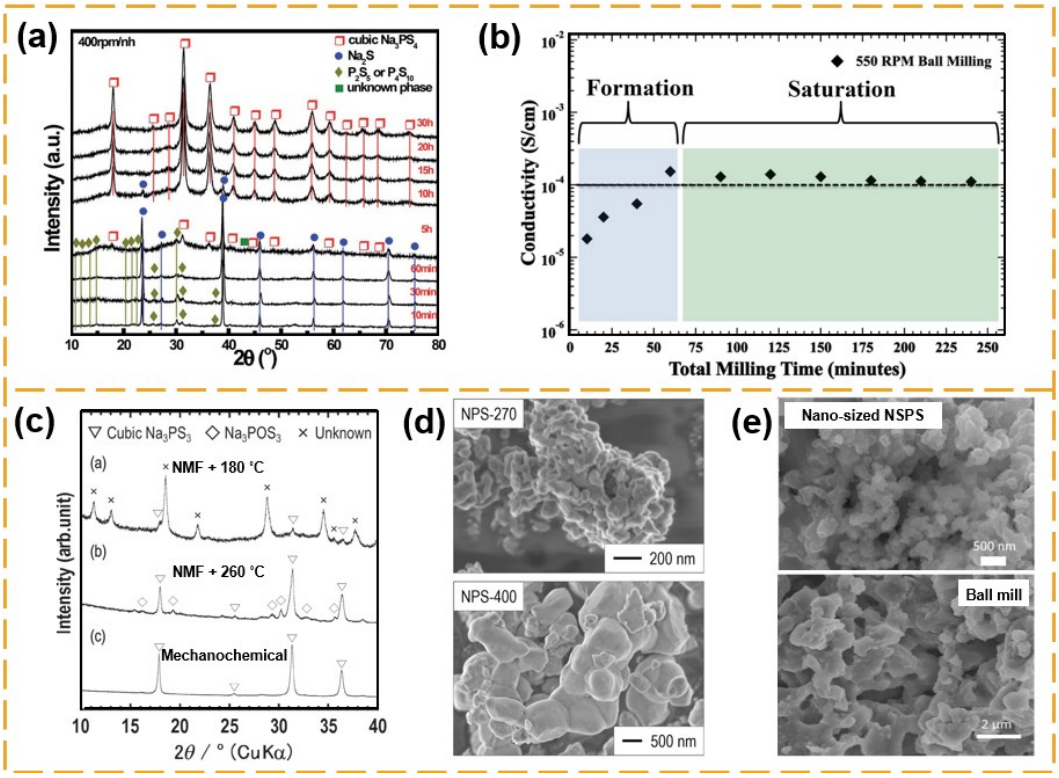

Figure 3. (a) Powder XRD patterns of $75Na_2S$-$25P_2S_5$ samples synthesized by ball milled (400 rpm, 30 h) and annealed at various temperatures. Reproduced with permission.[68] Copyright 2016, Royal Society of Chemistry. (b) conductivity of the ball-milled $75Na_2S$-$25P_2S_5$ mixture as a functional of total milling time at 550 rpm. Reproduced with permission.[69] Copyright 2019, Elsevier; (c) XRD patterns of Na_3PS_4 electrolytes prepared after different procedures: using NMF solvent and Na_3PS_4 prepared by mechanochemical method. Reproduced with permission.[89] Copyright 2015, Oxford University Press. (d) FE-SEM images of NPS-270 and NPS-400 particles; Reproduced with permission.[88] Copyright 2019, Elsevier. (e) SEM images of $Na_{11}Sn_2PS_{12}$ prepared by liquid phase and ball-milling methods, respectively. Reproduced with permission.[59] Copyright 2021, American Chemical Society.

2.2.2. Aqueous-based Synthesis

Na_3SbS_4 and doped conductors also can be synthesized by the wet-chemical method using water as the solvent.[54-56, 94] Jung et al. reported to mix Na_2S, Sb_2S_3, S in water and then washed with EtOH and heat-treated at 200 °C under vacuum to produce a pure tetragonal phase of Na_3SbS_4.[54] The aqueous-solution synthesized Na_3SbS_4 exhibited an impressive conductivity of 0.1-0.2 mS cm^{-1} at 25 °C. Later, Hayashi and co-workers synthesized $Na_{3-x}Sb_{1-x}W_xS_4$ (x = 0.09, 0.12, 0.15) conductors from aqueous solution by using Na_3SbS_4 and Na_2WS_4 as precursors, followed by drying at 150 °C and heating at 275 °C.[55] The produced

$Na_{2.88}Sb_{0.88}W_{0.12}S_4$ SE showed the highest ionic conductivity of 4.2 mS cm^{-1} at RT, which is higher than Na_3SbS_4 and Na_3PS_4 SEs that were synthesized with other solvents. In addition, the aqueous-based synthesis is also explored to introduce halogen dopants (Br^-, Cl^-) in Na_3SbS_4 to produce $Na_{3-x}SbS_{4-x}Cl_x$ ($0 \leq x \leq 0.1$),[56] and $Na_{3-x}SbS_{4-x}Br_x$.[94] For both Cl- and Br-doped Na_3SbS_4 SEs, the drying/heating temperatures are below 200 °C.

3. Crystal Structures and Conductive Properties

The polymorphs of glassy sulfides, Na_3PS_4, Na_3SbS_4 and $Na_{11}Sn_2PS_{12}$ SEs are reviewed in this session, including the glassy and crystalline materials. The conduction mechanisms and conductive properties of pure sulfide Na-ion conductors are also introduced. In addition, the doping effects of different dopants (anion or cation, aliovalent or isovalent) on the crystal structure and phase stability as well as the ionic conductivity are discussed. **Table 2** present a summary of synthesis methods, crystal structure, and conductive properties for these sulfide-type Na-ion conductors.

Table 2. Summary of synthesis methods, crystal structure, and conductive properties for Na_3PS_4, Na_3SbS_4 and $Na_{11}Sn_2PS_{12}$ SEs families

Composition	Structure	Synthesis method	Synthesis Temp	Ionic conductivity (S cm^{-1})	Activation energy	Ref
Na_3PS_4	cubic	mechanochemical	270 ˚C	4.6×10^{-4}	27 kJ mol^{-1}	[67]
Na_3PS_4	tetragonal	organic solvent method	400 ˚C	2.6×10^{-4}	-	[88]
$Na_{2.9375}PS_{3.9375}Cl_{0.0625}$	tetragonal	organic solvent method	480 ˚C	4.3×10^{-4}	25.4 kJ mol^{-1}	[88]
$Na_3PS_{3.8}Cl_{0.2}$	tetragonal	mechanochemical + solid reaction	420 ˚C	1.96×10^{-3}	0.19 eV	[47]
$94Na_3PS_4$-$6Na_4SiS_4$	cubic	mechanochemical	220 ˚C	7.4×10^{-4}	~ 25 kJ mol^{-1}	[95]
$71Na_3PS_4$-29NaI	-	mechanochemical	200-270 ˚C	1.5×10^{-5}	-	[82]
$Na_{2.9375}PS_{3.9375}Cl_{0.0625}$	tetragonal	solid-state reaction	800 ˚C	1.14×10^{-4}	0.249 eV	[96]
$Na_{2.73}Ca_{0.135}PS_4$	cubic	mechanochemical + solid-state reaction	700 ˚C	9.4×10^{-4}	0.346 eV	[44]
$Na_{2.85}P_{0.85}W_{0.15}S_4$	cubic	mechanochemical	550 ˚C	8.8×10^{-3}	21 kJ mol^{-1}	[70]
$Na_{2.85}P_{0.85}W_{0.15}S_4 + WS_2$	cubic + hexagonal	solid-state reaction	550 ˚C	1.3×10^{-2}	21 kJ mol^{-1}	[70]

$Na_3PS_{3.85}O_{0.15}$	tetragonal	mechanochemical	-	2.7×10^{-4}	41.5 kJ mol^{-1}	[50]
Na_3SbS_4	tetragonal	solid-state reaction	700 ˚C	3×10^{-3}	0.25 eV	[77]
Na_3SbS_4	tetragonal	decomposition	150 ˚C	1.05×10^{-3}	0.22 eV	[97]
Na_3SbS_4	tetragonal	organic solvent method	100 ˚C	2.3×10^{-4}	0.37 eV	[98]
Na_3SbS_4	tetragonal	aqueous solution method	100 ˚C	2.6×10^{-4}	0.32 eV	[98]
$Na_{3.75}Sn_{0.75}Sb_{0.25}S_4$	tetragonal	solid-state reaction	550 ˚C	5.1×10^{-4}	-	[80]
$Na_{3.6}Sn_{0.6}Sb_{0.4}S_4$	tetragonal	solid-state reaction	450 ˚C	3×10^{-4}	0.39 eV	[80]
Na_3SbS_4	cubic	solid-state reaction + mechanochemical	700 ˚C	2.8×10^{-3}	0.061 eV	[76]
Na_3SbS_4	tetragonal	aqueous solution method	200 ˚C	2.1×10^{-4}	0.27 eV	[54]
0.1NaI-0.9Na_3SbS_4	tetragonal	organic solvent method	150 ˚C	7.4×10^{-4}	~ 0.28 eV	[53]
Na_3SbSe_4	cubic	solid-state reaction	650 ˚C	8.5×10^{-4}	0.193 eV	[79]
$Na_{2.9}Sb_{0.9}W_{0.1}S_4$	cubic	solid-state reaction	550 ˚C	~4.1×10^{-2}	~ 0.19 eV	[81]
$Na_{2.88}Sb_{0.88}W_{0.12}S_4$	cubic	mechanochemical	275 ˚C	3.2×10^{-2}	17 kJ mol^{-1}	[49]
$Na_{2.88}Sb_{0.88}W_{0.12}S_4$	tetragonal	aqueous solution method	275 ˚C	4.28×10^{-3}	0.248 eV	[55]
$Na_{2.895}Sb_{0.7}W_{0.3}S_4$	orthorhombic	solid-state reaction	520 ˚C	2.42×10^{-2}	0.09 eV	[99]
$Na_{2.95}SbS_{3.95}Cl_{0.05}$	tetragonal	aqueous solution method	150 ˚C	9.0×10^{-4}	26.2 kJ mol^{-1}	[56]
$Na_{3.1}Ge_{0.1}Sb_{0.9}S_4$	tetragonal	mechanochemical + solid-state reaction	750 ˚C	5.1×10^{-3}	0.156 eV	[72]
$Na_{11}Sn_2PS_{12}$	tetragonal	solid-state reaction	600 ˚C	3.7×10^{-3}	0.383 eV	[83]
$Na_{11.1}Sn_{2.1}P_{0.9}Se_{12}$	tetragonal	solid-state reaction	600 ˚C	3.0×10^{-3}	0.30 eV	[100]
$Na_{10.8}Sn_{1.9}PS_{11.8}$	tetragonal	solid-state reaction	700 ˚C	6.7×10^{-4}	0.307 eV	[62]
$Na_{11}Sn_2PSe_{12}$	tetragonal	solid-state reaction	900 ˚C	2.15×10^{-3}	0.28 eV	[61]
$Na_{11}Sn_2PS_{12}$	tetragonal	organic solvent method	460 ˚C	1.73×10^{-4}	33 kJ mol^{-1}	[59]
$Na_{10.3}Sn_{1.3}P_{1.7}S_{12}$	tetragonal	mechanochemical	400 ˚C	3.0×10^{-4}	30 kJ mol^{-1}	[101]
$Na_{11.5}Sn_2Sb_{0.5}Ti_{0.5}S_{12}$	tetragonal	solid-state reaction	600 ˚C	1.01×10^{-3}	0.274 eV	[63]
$Na_{11}Sn_2PS_{12}$	tetragonal	Organic solvent method	550 ˚C	1.0×10^{-4}	0.42 eV	[86]

3.1. Glassy Sulfide Compounds

Na_3PS_4 has been reported as a glassy state (amorphous) and glass-ceramic that synthesized by using 75% Na_2S and 25% P_2S_5 precursors with ball milling process.[16] The crystallization behaviors of amorphous Na_3PS_4 have been studied *via in situ* TEM,[95] which reveals that the amorphous sample firstly changes to cubic and then to tetragonal structure as the temperature increases. Annealing temperatures strongly influence the crystal structures of Na_3PS_4.[68] **Figure 4a** shows the XRD patterns of Na_3PS_4 glass and the crystallization after heating. The mechanochemical reaction yields to Na_3PS_4 glass, as indicated by the absence of all diffraction peaks. After annealing at 270 °C, the cubic Na_3PS_4 phase is observed. In contrast, annealing at higher temperature of 420 °C results in the formation of the tetragonal Na_3PS_4 phase. The glass-ceramic Na_3PS_4 exhibits an impressive ionic conductivity of 0.2-0.46 mS cm^{-1} at room temperature (RT),[67] which triggers strong interests on studying sulfide-based Na-ion conductors. In 2018, nanosized Na_3SbS_4 crystallites surrounded with amorphous (disordered) domain was reported in xNaI·(1-x)Na_3SbS_4 SEs after heat treatment below 200 °C.[53] This fact is revealed by the high resolution TEM (HRTEM) image and fast Fourier transform (FFT) pattern in **Figure 4b**. The highest ionic conductivity is 0.74 mS cm^{-1} for 0.1NaI·0.9Na_3SbS_4. Recently, oxysulfide glass $Na_3PS_{4-x}O_x$ (NPSO) that using O^{2-} partial replacement of S^{2-} was successfully synthesized with $0 \leq x \leq 0.60$ (**Figure 4c**).[50] When x=0.15, the optimal composition $Na_3PS_{3.85}O_{0.15}$ exhibited the highest ionic conductivity of 0.27 mS cm^{-1} and lowest electronic conductivity (10^{-9} S cm^{-1}) than Na_3PS_4 SE.

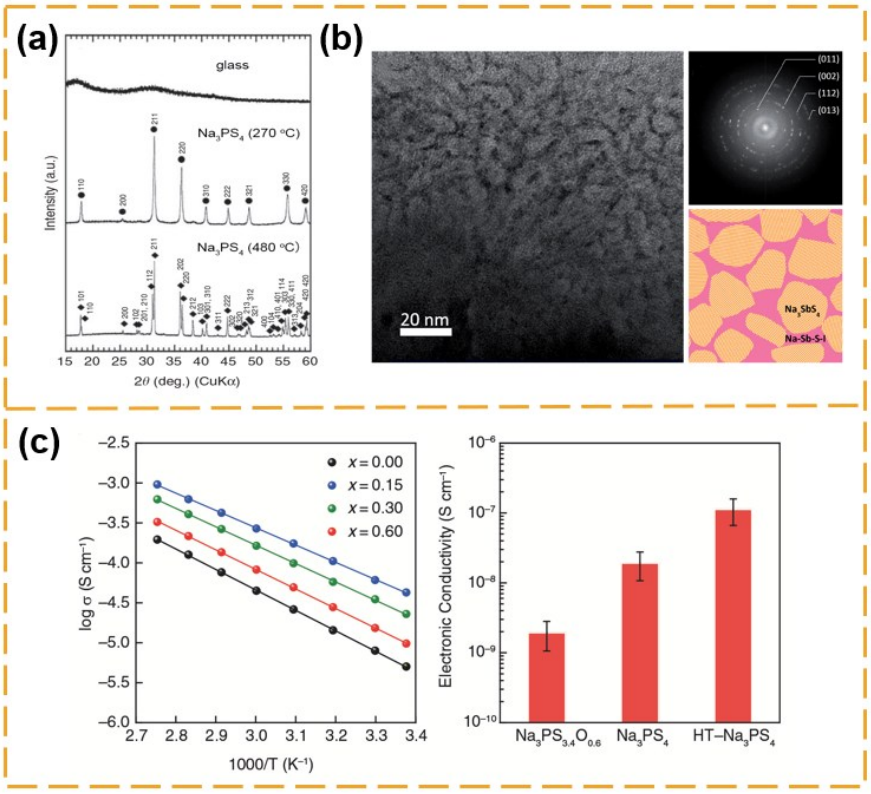

Figure 4. (a) XRD patterns of the Na_3PS_4 glass, glass-ceramic sample heated at 270 °C and 420 °C; Reproduced with permission.[35] Copyright 2012, Springer Nature. (b) HRTEM, FTT patterns and schematic of microstructures of glass-ceramic $0.1NaI{\cdot}0.9Na_3SbS_4$ from liquid synthesis. Reproduced with permission.[53] Copyright 2018, Royal Society of Chemistry. (c) Left: Temperature dependence of the Na-ion conductivities of SEs; right: Electronic conductivity of three types of SEs measured by two-blocking electrodes at 60 °C, error bars indicate the standard deviation of three tests. Reproduced with permission.[50] Copyright 2022, Springer Nature.

3.2. Na_3PS_4 Compounds

3.2.1. Pure Na_3PS_4: Crystal Structure and Conductivity

At the beginning, Na_3PS_4 was thought to have two polymorphs (**Figure 5a**): the tetragonal phase (space group $P\bar{4}2_1c$) and the cubic phase ($I\bar{4}3m$ space group).[16, 81, 96, 97] In the cubic Na_3PS_4, Na-ions (at 6b site) are located in the middle of the two PS_4^{3-} tetrahedra, and the PS_4^{3-} tetrahedra are arranged in a body-centered cubic (bcc) sublattice to construct the rigid matrix. As for the tetragonal structure Na_3PS_4, the Na(6b) site splits into two distinct sites of Na(2a) and Na(4d) due to a minor rotation of the PS_4^{3-} polyhedral,[66] and this rotation also results in the lattice parameter ratio *c*/*a* increases from unity. **Figure 5b** shows the comparison of Rietveld

refinements of XRD results for c-Na_3PS_4 (from mechanochemical method) and t-Na_3PS_4 (high temperature solid-state synthesis).[98] The lattice parameter of cubic-Na_3PS_4 is *a*=6.9893 Å while the lattice parameters of tetragonal-Na_3PS_4 are *a*=6.9528 Å, *c*=7.0973 Å. When the temperature is higher than 500 °C for Na_3PS_4, there is another phase transition from cubic to orthorhombic structure, the third polymorph. In the range of 35-550 °C, the structural evolution of Na_3PS_4 from tetragonal (α) to cubic (β) at 200-300 °C and from cubic (β) to orthorhombic (γ) at 500-530 °C can be clearly observed in temperature-dependent Bragg diffraction in **Figure 5c**.[99] The synchrotron XRD patterns of γ-Na_3PS_4 at 550 °C are indexed into an orthorhombic structure (*Fddd* space group) with lattice parameters of *a*=6.6055(1) Å, *b*=11.7143(2) Å, and *c*=20.7378(3) Å. This proposed structure of γ-Na_3PS_4 is displayed in **Figure 5d** based on the static *ab initio* calculations.[100] The relative occupancies of Na sites were approximated from the relative calculated energies of different configurations. In addition, unlike the tetragonal-to-cubic phase change, the cubic-to-orthorhombic phase transition involved a distinct change in PS_4^{3-} bonding as well as an abrupt increase in the volume of the unit cell.[99]

The Na_3PS_4 glass-ceramic was first reported to show a higher ionic conductivity (0.2 mS cm^{-1}) than that of the tetragonal structured Na_3PS_4 (0.01 mS cm^{-1}).[16] However, theoretical calculations showed that both of cubic and tetragonal phases with the exact stoichiometric ratio have poor ionic conductivity.[66] The activation energy of Na-ion diffusion in cubic and tetragonal structure were also very similar, 0.19 eV for cubic and 0.20 eV for tetragonal, respectively.[68] Therefore, instead of crystal structure itself, other local scale factors such as defect concentration (i.e. vacancies) and microstructure (i.e. grain boundary) are more likely responsible for the distinct on ionic conductivity in tetragonal and cubic structures. For the defect such as vacancies, Wagemaker et al. performed molecular dynamics simulations and demonstrated the dramatic difference on Na vacancy densities between Na_3PS_4 and $Na_{2.94}PS_4$ (with 2% concentration of vacancy), indicating that introducing vacancies has a large influence

on the conductivity.[66] For cubic Na_3PS_4, the vacancy distribution and concentration also influence the grain boundary resistance.[101]

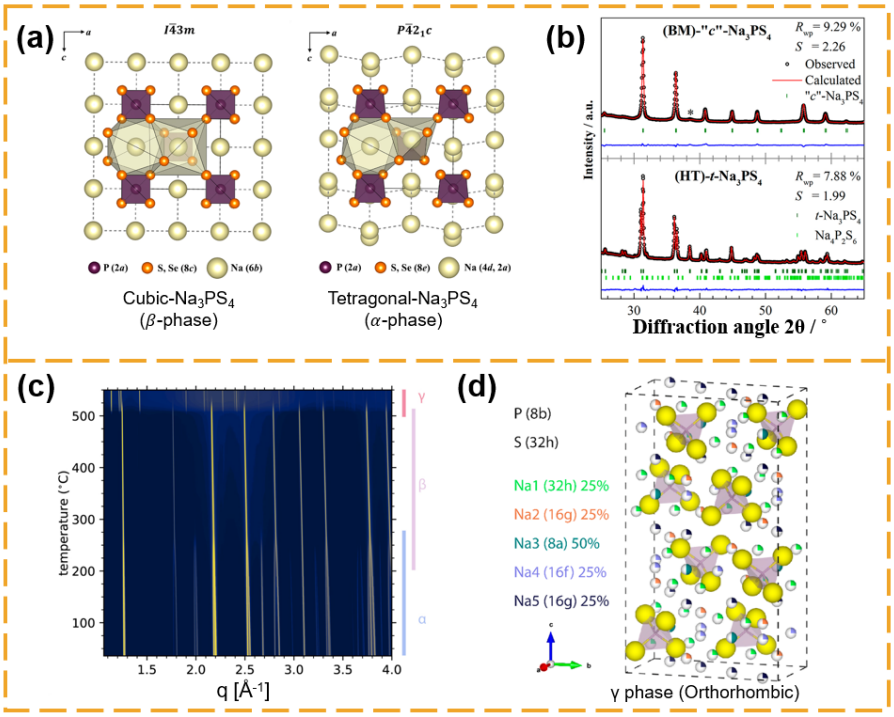

Figure 5. (a) Unit cell of the cubic and tetragonal of Na_3PCh_4 with Ch = S, Se. Reproduced with permission.[97] Copyright 2018, American Chemical Society. (b) Rietveld refinements of X-ray diffraction data for (BM)-"c"- Na_3PS_4 and HT-t-Na_3PS_4. Reproduced with permission.[98] Copyright 2018, American Chemical Society. (c) Contour plot of the X-ray Bragg diffractograms as a function of temperature for Na_3PS_4 in the range of 35-550 °C. Reproduced with permission.[99] Copyright 2021, American Chemical Society. (d) Proposed structure of *γ*-Na_3PS_4 from static *ab initio* calculation. P and S in purple and yellow, respectively. Reproduced with permission.[100] Copyright 2019, American Chemical Society.

3.2.2. Doping Effect on Crystal Structure and Conductivity of Na_3PS_4

Olivier et al. combined quasi-elastic neutron scattering (QENS) experiments and AIMD simulations to study the atomic dynamics in Na_3PS_4 within a wide temperature range (100-600 K).[102] The temperature evolution of experimental QENS spectra and the fitted results (**Figure 6a**) showed that the estimated Na-ion jump length is 3.6 Å and the diffusion coefficient D is on the order of 10^{-6} cm^2 s^{-1} at 600K, which is typical for superionic conductors. Beside temperature, applied external pressure could also decrease the impedance and improve the ionic conductivity

of tetragonal (HT) Na_3PS_4 by 10 times higher due to the proposed consolidation mechanism.[65] Due to the doping effects on the crystal structure, both cation and anion doping strategies are effective to enhance the ionic conductivity of Na_3PS_4, in specific, cation introducing interstitials and anion bring in additional vacancies.

Cation Substitution for P^{5+} in Na_3PS_4. The Group IVA elements such as Si and Ge have been studied for the partial substitution of P in Na_3PS_4 structure. The initial attempt was reported for introducing 6 mol% of Si into glass-ceramic Na_3PS_4 to push up the RT ionic conductivity from 0.25 mS cm^{-1} to 0.74 mS cm^{-1} for 0.94 Na_3PS_4·0.06 Na_4SiS_4.[103] Later, the theoretical simulations also predicted that 6.25 mol% Si- and 6.25 mol% Sn-doped cubic Na_3PS_4 could show achieve the RT conductivity of 1.66×10^{-3} S cm^{-1} and 1.07×10^{-2} S cm^{-1}, respectively.[104] The enhanced conductivity by Si doping is explained by the fact that the excess Na^+ ions lead to the increased occupancy in the interstitial Na2 site and thus promote the ion transport. In the other work, Adams et al. systematically investigated the doping effect (x=0.1) of the other Group IVA elements (Ge, Ti, and Sn) on the $Na_{3+x}Sn_xP_{1-x}S_4$ SEs (**Figure 6b**).[105] They found that all dopants increased the lattice volume due to the added Na interstitials with the sequence Si<Ge<Ti<Sn, same as the atomic radii of the dopants. Meanwhile, the average site energies of the Na ions decreased in the reverse order, with the Sn doping appeared the most promising. And the experimental results showed that $Na_{3.1}Sn_{0.1}P_{0.9}S_4$ achieved the highest ionic conductivity of 0.25 mS cm^{-1} at RT. Besides, other cations such as As and W were also attempted to introduce into Na_3PS_4 structure to achieve even higher ionic conductivity.[81, 106] For instance, $Na_3P_{0.62}As_{0.38}S_4$ was reported to exhibit a high RT ionic conductivity of 1.46 mS cm^{-1} and enhanced moisture stability;[106] cubic $Na_{2.9}P_{0.9}W_{0.1}S_4$, were discovered to achieve an ultra-high ionic conductivity of 13 mS cm^{-1}.[81]

Cation Doping to Replace Na^+ in Na_3PS_4. Instead of the replacement of P, the other cation doping strategy is to partially substitute Na^+ in Na_3PS_4 SE by aliovalent cations such as Ca^{2+}.

In 2018, cubic $Na_{3-2x}Ca_xPS_4$ conductors were explored by introducing Ca^{2+} into tetragonal Na_3PS_4 to replace Na^+ at Na(12d) site.[44] Ca-doping not only stabilized the cubic phase at RT but also created additional Na vacancies to promote Na-ion diffusion. The Ca-doping content influenced the ionic conductivity of $Na_{3-2x}Ca_xPS_4$ SEs (**Figure 6c**) and the highest value of 1 mS cm^{-1} was achieved for $Na_{2.73}Ca_{0.135}PS_4$ (x=0.135). In the other work, Cai et al. calculated the generation energy for tetragonal and cubic crystal structures under various Ca-doping concentrations. With a lower Ca-dopant content, the cubic structure is more stable for $Na_{2.75}Ca_{0.125}PS_4$ (x=0.125) while the tetragonal structure has lower generation energy for $Na_{2.5}Ca_{0.25}PS_4$ (x=0.25).[107]

Aliovalent Anion Doping for S^{2-} in Na_3PS_4. The aliovalent substitution of S^{2-} by halogen ions (X^-, X=F, Cl, Br, I) also can create Na vacancies in Na_3PS_4 due to the charge neutrality and therefore influence on the ionic diffusivity.[47, 108] In 2016, Ong et al. successfully synthesized Cl-doped t-Na_3PS_4 and found the optimal composition of t-$Na_{2.9375}PS_{3.9375}Cl_{0.0625}$ to achieve the high ionic conductivity of 1.14 mS cm^{-1} at 30 °C and a low activation energy of 0.249 eV.[109] Such high ionic conductivity is ascribed to the formation of a 3D diffusion network consists of Na(1) sites along the c direction interconnected via the Na(2) sites, as shown in the Na^+ probability density distribution (**Figure 6d**). Using first-principal calculations to compare different halogen ions, Zhang et al. reported that Cl^- exhibited good chemical compatibility with the S^{2-} host due to the similar ionic radius, while Br-doped t-Na_3PS_4 (t-$Na_{47}P_{16}S_{63}Br$) showed the lowest activation and the highest Na ionic conductivity of 2.37 mS cm^{-1} at 300K.[110] For halogen ions, if the doping content is too high, an impurity phase formed and caused the decrease of conductivity, for instance, when x>0.1 for (1-x)Na_3PS_4·xNaI glass.[82]

Iso-valent Anion Substitution of S^{2-} in Na_3PS_4. Isovalent anions such as Se^{2-} and O^{2-} also have been explored to substitute S^{2-} in Na_3PS_4 to affect Na-ion diffusion. In 2016, Ceder et al. predicted and synthesized Na_3PSe_4 with cubic structure, which achieved ionic conductivity of

0.11 mS cm^{-1} at RT.[111] Then they also studied the $Na_3PS_xSe_{4-x}$ SEs and observed the variations of ionic conductivity as well as the activation energy as increasing Se-content.[43] In another work, the increase of Se-doping content was found to soften the lattice, and thus decreases the activation barrier for ion motion.[97]

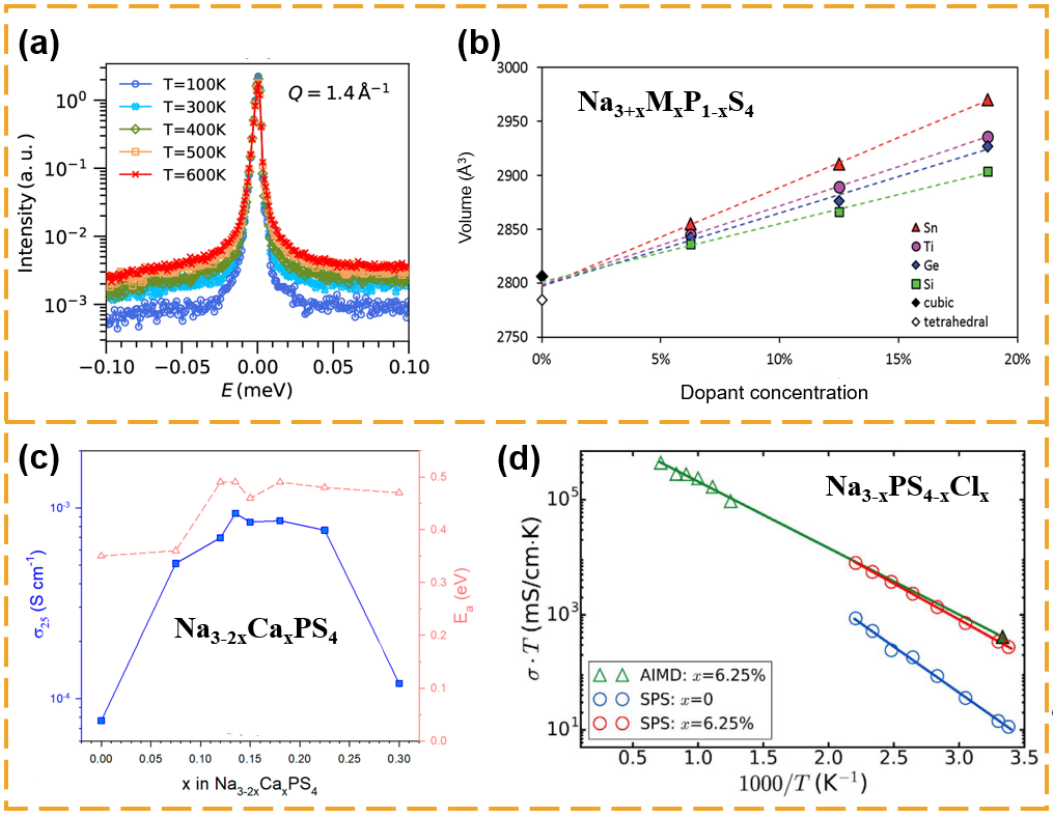

Figure 6. (a) Temperature dependent QENS spectra of Na_3PS_4, measured at Q=1.4 Å^{-1}. The measured Q-dependence of Γ (orange markers) fitted with Chudley-Elliot jump-diffusion model (solid line); Reproduced with permission.[102] Copyright 2021, Royal Society of Chemistry. (b) Volume of $Na_{3+x}M_xP_{1-x}S_4$ phases versus dopant concentration x in percent based on DFT geometry optimization. Reproduced with permission.[105] Copyright 2017, Royal Society of Chemistry. (c) Na-ion conductivities at 25 °C and activation energies for $Na_{3-2x}Ca_xPS_4$. Nyquist plots are shown in the inset. Reproduced with permission.[44] Copyright 2018, American Chemical Society. (d) Arrhenius plots of the t-$Na_{3-x}PS_{4-x}Cl_x$ with x = 0 (blue) and 6.25% (red) obtained from spark plasma sintering (SPS) experiments, and x = 6.25% (green) from AIMD simulations. Reproduced with permission.[109] Copyright 2016, Springer Nature.

3.3. Na_3SbS_4 Compounds

3.3.1. Pure Na_3SbS_4: Crystal structure and conductivity

Na_3SbS_4 shows two crystalline phases: cubic and tetragonal. The low-temperature phase, tetragonal Na_3SbS_4 (space group $P\bar{4}2_1c$), was reported by three groups in 2016.[18, 51, 52] As shown in **Figure 7a**, the unit cell consists of two SbS_4 tetrahedron groups (with Sb atoms on 2b sites and S atoms on 8e sites). There are two main Na sites: Na(1) in a NaS_6 distorted octahedron, and Na(2) in a NaS_8 dodecahedron. The Na(1) and Na(2) sites are alternatively arranged in the a-b plane while the Na(1)-Na(1) path is along the c-direction. They construct a 3D ion diffusion network in t-Na_3SbS_4. Both neutron diffraction and X-ray diffraction confirmed the existence of Na vacancies in t-Na_3SbS_4 lattice (mostly at Na(2) sites), which play significant roles to facilitate Na-ion transport.[18, 51] The tetragonal structure of Na_3SbS_4 was observed to be stable under high pressure.[112] For the high-temperature phase (cubic, space group of $I\bar{4}3m$), the Na sites are identical. Cubic-structured Na_3SbS_4 had been reported to be stabilized at lower temperatures by the controlled synthesis method.[76] For solid-state reaction synthesis, *in situ* neutron diffraction results (**Figure 7b**) revealed that the direct formation of cubic-Na_3SbS_4 at the temperature range of 300-350 °C from precursors of Na_2S, Sb_2S_3 and S.[113] When heating up t-Na_3SbS_4, a tetragonal-to-cubic phase transition occurred.[76, 114] Meanwhile, as the temperature drops, the cubic phase would transition back to tetragonal phase at 150-180 °C .

The ionic conductivity of tetragonal Na_3SbS_4 is depended on the synthesis approaches. It varies from 1-3 mS cm^{-1} by dry synthesis[18, 115] to 0.1-0.5 mS cm^{-1} by liquid-phased method.[54] In pure Na_3SbS_4, Na vacancies play an important role on its high ionic conductivity.[18, 51] In tetragonal Na_3SbS_4,there are two main sites for Na atoms in the lattice: Na(1) in a NaS_6 distorted octahedron, and Na(2) in a NaS_8 dodecahedron (**Figure 7c**). The 3D tunnel network for Na^+ ion transport is constructed by the combination of a planar pathway and an interplane chain pathway.[18, 114-116] In the *ab*-plane, the NaS_6 and NaS_8 sites are alternatively arranged and are connected by shared faces to form planar tunnel network of -Na(1)-Na(2)-Na(1)-Na(2)- to

enable ion transport, meanwhile, the NaS_6 octahedra are mutually linked with shared edges along the *c*-axis to allow Na^+ to hopping across the planar network. The activation energy barrier in tetragonal Na_3SbS_4 is estimated to be 0.22 eV, while the value dramatically decreases to 0.036 eV for cubic structured Na_3SbS_4 (**Figure 7d**).[114] Zhang and co-workers attempted different synthesis approaches to stabilize cubic-structured Na_3SbS_4, and observed the distinct activation energy for cubic (0.06 eV) and tetragonal structure (0.25 eV).[76]

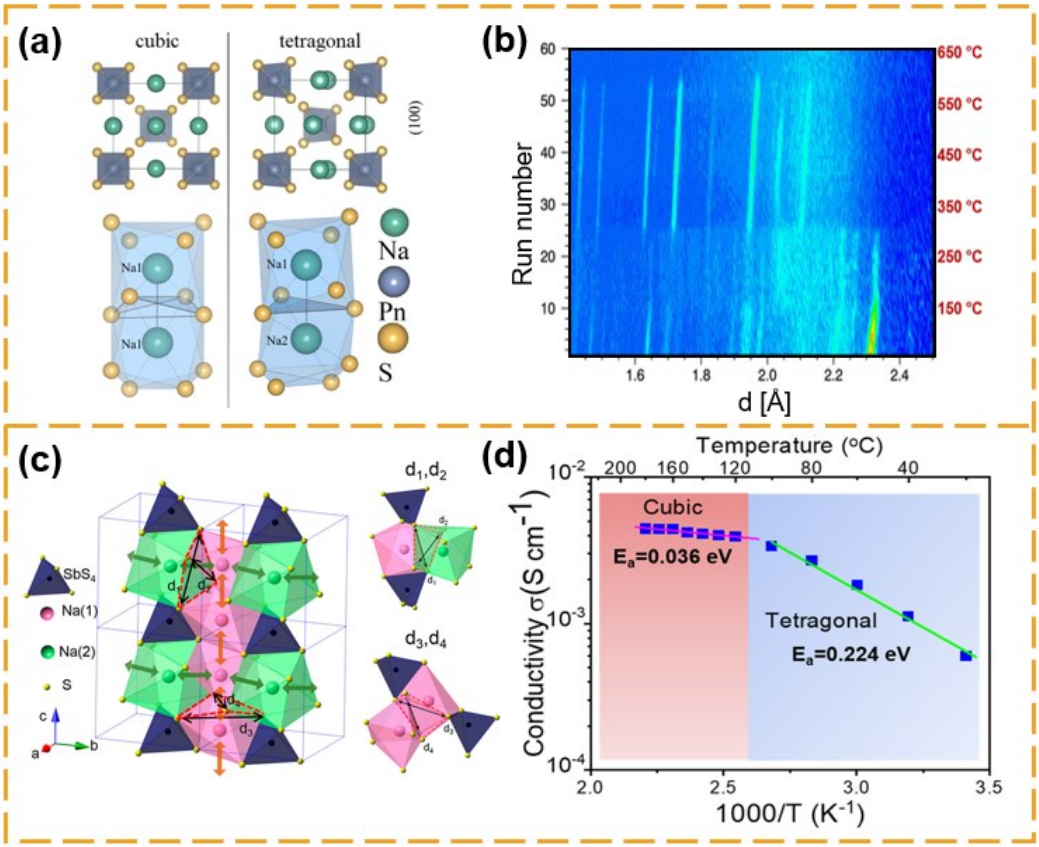

Figure 7. (a)Unit cells of the cubic and tetragonal Na_3PnS_4 with Pn=P, Sb. A full Na^+ occupancy within the direct diffusion pathway. Reproduced with permission.[81] Copyright 2020, American Chemical Society. (b)Visual plots of in-situ neutron diffraction for heating process of Na_3SbS_4 from precursor mixtures (Na_2S, Sb_2S_3, S); Reproduced with permission.[113] Copyright 2021, Wiley-VCH. (c)Structure of the tetragonal Na_3SbS_4 framework with conduction paths of Na(1)-Na(1) (along the z-axis) and Na(1)−Na(2) (in the xy-plane). The right schematic display is magnified to show the S gates (d1, d2, d3, d4). Reproduced with permission.[114] Copyright 2018, American Chemical Society. (d)Arrhenius plot of Na_3SbS_4 in the temperature range of 20−180 °C. Reproduced with permission.[117] Copyright 2020, American Chemical Society.

3.3.2. Doping Effects on Crystal Structure and Conductivity of Na_3SbS_4

Different types of dopants including anion or cations have been studied to introduce into Na_3SbS_4 and influence its crystal structure. Similar to Na_3PS_4, different types of anion or cation dopants have been introduced into tetragonal Na_3SbS_4. The doping factors such as anion/cation, aliovalent/iso-valent, concentration and the synthesis approaches for doping process all show dramatic influence its ionic conductivity.

Cation Doping on Na_3SbS_4 Compounds. With rich Sn dopant, $Na_{3.75}S_{0.75}Sb_{0.25}S_4$ was found to crystallize in a tetragonal phase with space group of $I4_1/acd$.[80] X-ray diffraction and Rietveld refinement (**Figure 8a**) revealed the lattice parameters a =13.829 Å and c =27.518 Å. The unit cell contains one Sn site, one Sn/Sb mixed site, three S sites and five Na sites. Introducing Ge into Na_3SbS_4 resulted in the expansion of the unit cell due to the existence of interstitial sodium defects.[72] For W doping, it was found that the decrease of tetragonal distortion in $Na_{3-x}Pn_{1-x}W_xS_4$ (Pn=Sb, P, x<0.125) lattice as the W content was increased.[81] In another work, $Na_{2.88}Sb_{0.88}W_{0.12}S_4$ showed a cubic structure (a = 7.1920(1) Å, $I\bar{4}3m$), and the unit cell consisted of a body-centered sublattice of SbS_4^{3-} and WS_4^{2-} (confirmed by W-S bonds in Raman spectra).[49] Moreover, the aliovalent W-doping also generates additional Na vacancies in the lattice, which contributes to its high ionic conductivity of $Na_{2.88}Sb_{0.88}W_{0.12}S_4$ SE. Heavily W-doping (x=0.3) was also studied in $Na_{2.7}Sb_{0.7}W_{0.3}S_4$.[57] This SE exhibits a very slight orthorhombic lattice distortion from the cubic structure. The lattice parameters a =14.3762 Å, b =14.3757 Å and c =14.3774 Å was characterized via the synchrotron XRD and Rietveld refinement (**Figure 8b**), and DFT further optimized the lattice parameters with more distortions. With the same W-doping content, $Na_{2.895}Sb_{0.7}W_{0.3}S_4$ with excess Na showed the cubic structure and higher ionic conductivity (24.2 mS cm^{-1}).

The partial substitution of W or Sn to Sb in Na_3SbS_4 has attracted strong research interests.[55, 57, 80, 118] For W dopant, Hayashi et al. reported that an optimal composition of cubic $Na_{2.88}Sb_{0.88}W_{0.12}S_4$ exhibited record high ionic conductivity of 32 mS cm^{-1} in 2019.[49] The fast

Na-ion transport is due to the generation of Na vacancies and the stabilization of cubic phase by introducing W^{6+} to facilitate the isotropic 3D fast ion conduction. Later, they also demonstrated to use of an aqueous solution approach to synthesize Na_3SbS_4–Na_2WS_4 to achieve an impressive ionic conductivity of 4.28 mS cm^{-1} at 25 °C.[55] In addition, $Na_{3x}Sb_{1-x}W_xS_4$ conductors with heavily W-doping content were also explored.[57] When x=0.3, $Na_{2.7}Sb_{0.7}W_{0.3}S_4$ SE exhibited high ionic conductivity of 14.5 mS cm^{-1}. It had a novel orthorhombic crystal structure that holds 3D ionic diffusion pathways. $Na_{2.895}Sb_{0.7}W_{0.3}S_4$ SE with excess Na-ion further improved the RT conductivity to 24.2 mS cm^{-1}. Zeier et al. compared the influence of the substitution with WS_4^{2-} for $PS_4^{3-}$and SbS_4^{2-} in Na_3PhS_4 (Ph=P, Sb) as increasing the vacancy concentration (**Figure 8c**).[81] With increasing vacancy content, the conductivity changed drastically alongside a continuous decrease of the activation barrier. $Na_{2.9}Sb_{0.9}W_{0.1}S_4$ showed a high ionic conductivity of 41 ± 8 mS cm^{-1}, in comparison to that of $Na_{2.9}P_{0.9}W_{0.1}S_4$ (13 mS cm^{-1}). Recently, W dopant combined with the second anion or cation doping has been studied to create more vacancies. For examples, Na_3SbS_4–$Na_2W_{0.77}S_4I_{0.6}$ glass-ceramic was reported to show RT ionic conductivity of 4.97 mS cm^{-1};[73] the W^{6+}/Si^{4+} co-doped $Na_{2.88}(W_{0.22}Si_{0.10}Sb_{0.68})S_4$ was found to show the conductivities of 20.2 and 7.4 mS cm^{-1} at RT and -20 °C, respectively.[119]

Anion Doping on Na_3SbS_4 Compounds. With larger radii size, the substitution of Se^{2-} for S^{2-} in Na_3SbS_4 can enlarge the unit cell. In the series of $Na_3SbS_{4-x}Se_x$ (x=0, 0.25, 0.5), the shift of diffraction peak indicates the lattice expansion as increasing the Se-doping content.[93] Another study of $Na_3SbS_xSe_{4-x}$ SEs shows the tetragonal to cubic phase transition as increasing the Se content.[79] Na_3SbS_3Se, $Na_3SbS_2Se_2$, and Na_3SbSSe_3 showed cubic structure ($I\bar{4}3m$ space group) with a = 7.420(5) Å, 7.346(4) Å and 7.271(7) Å, respectively, while Na_3SbS_4 had tetragonal space group $P\bar{4}2_1c$ with a slightly elongated c-axis (a = 7.163(3) Å, c = 7.295(3) Å and c/a = 1.018). Doping halogen (Cl, Br, I), the crystal structure changes differently due to the ionic

sizes (Cl<S<Br<I). In the lattice structure of $Na_{2.95}SbS_{3.95}Cl_{0.5}$ SE, the *a*-axis is slightly elongated while the *c*-axis shrinks, which reduces the lattice tetragonal distortion.[56] Due to the large ionic size, the lattice volume is expanded while the tetragonal structure retains after Br doping.[94] If the halogen dopant concentration is too high, an impurity phase such as NaX (X=Cl, Br, I) would appear in addition to Na_3SbS_4 phase.[53]

When using Se to replace S in Na_3SbS_4, the ionic conductivity of Se-doped Na_3SbS_4 SE is strongly dependent on the doping content and synthesis approaches.[79, 93] Chen et al. reported the $Na_3SbS_xSe_{4-x}$ (x=0, 1, 2, 3, 4) with distinct ionic conductivities but similar activation energy as varying Se-concentration.[79] For the same Se doping concentration ($Na_3SbS_{3.75}Se_{0.25}$), Wang et al. found that the synthesis methods strongly influenced the ionic conductivity.[93] In specific, as shown in **Figure 8d**, the liquid-solid fused synthesized sample showed a higher ionic conductivity (4.03 mS cm^{-1}) and lower activation energy (21.73 kJ mol^{-1}) than those samples from other methods: liquid- (28.89 kJ mol^{-1}) and solid-synthesis (31.14 kJ mol^{-1}).

The doping effects of halogen ions (Cl^-, Br^-, I^-) on tetragonal Na_3SbS_4 also have been studied.[53, 56, 94] For Cl^- dopant, Matsuda et al. reported the synthesis of $Na_{3-x}SbS_{4-x}Cl_x$ ($0 \leq x \leq 0.1$) SEs via a liquid-phase method.[56] Both the ionic conductivity and activation energy are dependent on doping concentration, and $Na_{2.95}SbS_{3.95}Cl_{0.05}$ (Cl content = 1.25%) achieved the highest ionic conductivity of 0.9 mS cm^{-1} at RT. When using the aqueous synthesis approach, the RT ionic conductivity of Cl-doped Na_3SbS_4 also increased as increasing the Cl concentration ($0 \leq x \leq 0.15$).[120] Similar to Cl^-, $Na_{3-x}SbS_{4-x}Br_x$ SEs with Br-doping were also synthesized via the aqueous solution method with adjustable Br concentration.[94] The optimal composition $Na_{2.76}SbS_{3.76}Br_{0.24}$ exhibited the highest ionic conductivity of 0.31 mS cm^{-1}. The glass-ceramic $0.1NaI{\cdot}0.9Na_3SbS_4$ was also reported to show enhanced ionic conductivity of 0.74 mS cm^{-1} than pure Na_3SbS_4 (0.34 mS cm^{-1}).[53] The increased ionic conductivity in halide-doped

Na_3SbS_4 is related with the created Na vacancies and distorted structure to facilitate Na^+ ion transport.

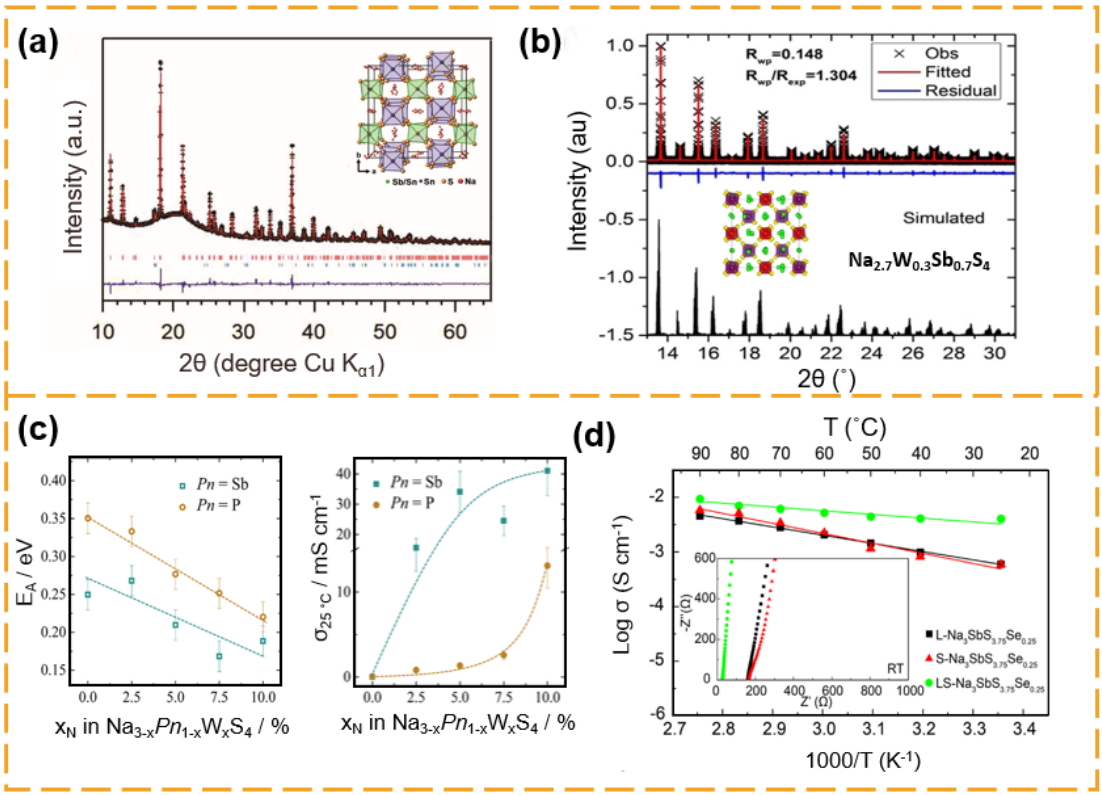

Figure 8. (a) Observed and calculated powder X-ray Rietveld refinement profile for $Na_{3.75}Sn_{0.75}Sb_{0.25}S_4$ recorded at 25 °C. Inset: crystal structure of $Na_{3.75}Sn_{0.75}Sb_{0.25}S_4$ (001) view. Reproduced with permission.[80] Copyright 2018, Wiley-VCH. **(b)** Up: Synchrotron XRD of $Na_{2.7}W_{0.3}Sb_{0.7}S_4$ and the Rietveld refinement based on an orthorhombic structure. Bottom: DFT simulated diffraction patterns. (Inset: Theoretically identified ground-state structure of $Na_{2.7}W_{0.3}Sb_{0.7}S_4$). Reproduced with permission.[121] Copyright 2021, Wiley-VCH. (c)Activation barriers of and room-temperature conductivities of $Na_{3-x}Pn_{1-x}W_xS_4$ with Pn = P, Sb. Reproduced with permission. [81] Copyright 2020, American Chemical Society. (d) Arrhenius conductivity plots of $Na_3SbS_{3.75}Se_{0.25}$ electrolytes. (The inset displays the impedance spectra of $Na_3SbS_{3.75}Se_{0.25}$ electrolytes at RT). Reproduced with permission.[93] Copyright 2019, Elsevier.

3.4. $Na_{11}Sn_2PS_{12}$ Compounds

3.4.1. Pure $Na_{11}Sn_2PS_{12}$: Crystal structure and conductivity

In consist with $Li_{10}GeP_2S_{12}$ (LGPS), quaternary sulfide-based $Na_{10}GeP_2S_{12}$ was firstly predicted with a space group of $P4_2/nmc$.[122, 123] However, following the stoichiometry ratio,

the synthesized $Na_{10}SnP_2S_{12}$ showed totally different diffraction patterns with LGPS, although it shows an impressive conductivity of 0.4 mS cm^{-1}. [124] After tailoring the Sn/P ratio from 1:2 (in $Li_{10}SnP_2S_{12}$) to 2:1, the pure phase $Na_{11}Sn_2PS_{12}$ was obtained, which shows a tetragonal structure (space group of $I4_1/acd$) with a = 13.6148(3) Å and c = 27.2244(7) Å (**Figure 9a and b**).[83] In this tetragonal structure, Sn and P form a tetrahedron with S, and then stack to construct the rigid matrix with Na ions distributed over six different Wyckoff positions: Na1(32g), Na2(16f), Na3(16c), Na4(16d), Na5(16e), Na6(8b). The Raman spectra of $Na_{11}Sn_2PS_{12}$ showed the symmetric stretches of the Sn-S and P-S bonds while a slightly shift when compared to the Na_3PS_4 and Na_3SnS_4 sulfides.[125] The other composition of $Na_{10.8}Sn_{1.9}PS_{11.8}$ showed the same $I4_1/acd$ structure with lattice parameters a =13.5876(12) Å and c = 27.155(5) Å, and a large number of Na-vacancies.[62]

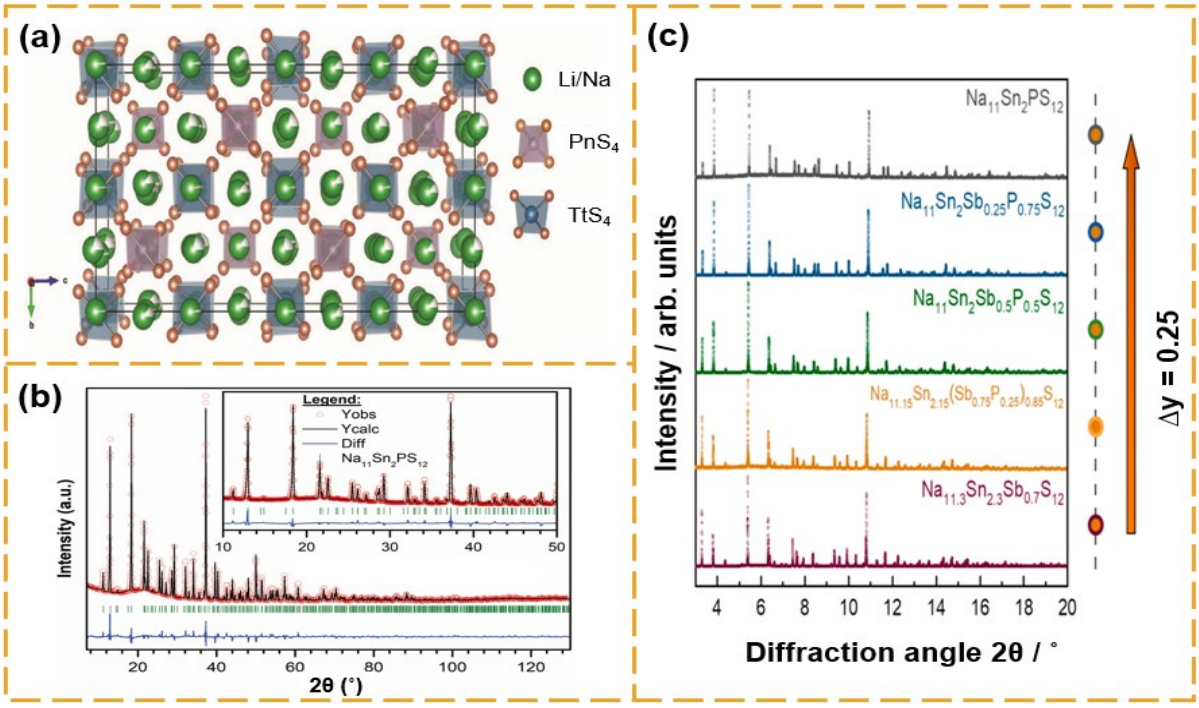

Figure 9. (a) Crystal structure of $Na_{11}Tt_2PnS_{12}$, Tt = Si/Ge/Sn, Pn =P/As/Sb. Purple tetrahedrons, PnS_4; blue tetrahedrons, TtS_4; green spheres, Li/Na. Reproduced with permission.[130] Copyright 2021, Wiley-VCH. (b) Rietveld refinement of X-ray powder diffraction data of single phase polycrystalline $Na_{11}Sn_2PS_{12}$. The insert shows an enlarged view. Reproduced with permission.[58] Copyright 2018, Royal Society of Chemistry. (c) All synchrotron diffractograms of the series $Na_{11+x}Sn_{2+x}(Sb_{1-y}P_y)_{1-x}S_{12}$. Reproduced with permission.[84] Copyright 2020, American Chemical Society.

The pure phase of $Na_{11}Sn_2PS_{12}$ with the tailored Sn/P of 2:1 was successfully synthesized in 2017, which showed a high ionic conductivity of 3.7 mS cm^{-1} (annealed sample) and 1.4 mS cm^{-1} (cold-pressed sample).[83] The high ionic conductivity of $Na_{11}Sn_2PS_{12}$ results from the vacancies and 3D network of Na^+ migration pathways. Before this discovery, $Na_{10}MP_2S_{12}$ (M=Sn, Si, Ge) has been predicted to be a 1D ion conductor by AIMD simulations (**Figure 10a**).[124] The experimentally synthesized $Na_{10}SnP_2S_{12}$ contained some impurity phases, but still exhibited an impressive ionic conductivity of 0.4 mS cm^{-1}. In $Na_{11}Sn_2PS_{12}$ structure, Na vacancies were reported to play important roles to interconnect for ion migration in 3D manner (**Figure 10b**), contributing to the high conductivity of close to 4 mS cm^{-1}.[83] Moreover, the Nyquist plot at -100 °C indicated that the resistance from grains was much higher than grain boundary resistance. In the other work by Nazar et al., they reported the impact of anion rotation on cation (Na^+) transport by transiently opening the triangular window in the NaS_6 octahedral cages.[126] In addition, Wang et al. also reported the synthesis of $Na_{10.8}Sn_{1.9}PS_{11.8}$ that containing larger numbers of vacancies.[62] This compound showed a great ionic conductivity of 0.67 mS cm^{-1} at 25 °C and an activation energy of 0.307 eV (**Figure 10c**), lower than that of 0.387 eV for $Na_{11}Sn_2PS_{12}$ in the previous work.[83] In comparison, the $Na_{11}Sn_2PS_{12}$ from liquid synthesis (after heat treated at 460 °C for 4 hours) was reported to exhibit a lower ionic conductivity of 0.173 mS cm^{-1} but comparable activation energy of 33 kJ mol^{-1}.[59]

3.4.2. Doping Effects on Crystal Structure and Conductivity of $Na_{11}Sn_2PS_{12}$

Anion Substitution/Doping in $Na_{11}Sn_2PS_{12}$. For the anion substitution of S^{2-} by Se^{2-}, $Na_{11.1}Sn_{2.1}P_{0.9}Se_{12}$ with a slightly off-stoichiometric composition was reported with an expanded host lattice.[84]In another work, $Na_{11}Sn_2PSe_{12}$ was found to have the tetragonal structure with $I4_1/acd$ space group, which has considerable Na vacancies and expanded lattice parameters (a =13.25Å, c = 28.41Å).[61] In the other study of Se/Sb co-doping study, the XRD patterns of $Na_{11}Sn_2SbS_{12-x}Se_x$ well matched $Na_{11}Sn_2SbS_{12}$ except that the peak shifts to lower

diffraction angles, indicating an increase of lattice parameters induced by Se substitution (with larger atomic radius than S). [75]

When using Se to replace S in quaternary Na-Sn-P-S system, $Na_{11.1}Sn_{2.1}P_{0.9}Se_{12}$ was first found to show a similar ionic conductivity of 3.0 mS cm^{-1} (vs. 3.7 mS cm^{-1} for $Na_{11}Sn_2PS_{12}$) but a considerably lower activation energy of 0.3 eV (*vs.* 0.39eV for $Na_{11}Sn_2PS_{12}$).[125] In addition, Wang et al. reported $Na_{11}Sn_2PSe_{12}$ conductor exhibited a grain ionic conductivity of 3.04 mS cm^{-1} and a total ionic conductivity of 2.15 mS cm^{-1},[61] which was 3 times higher than $Na_{11}Sn_2PS_{12}$ from the same group. The increased conductivity can be explained by the stretching force constants for Na-X (X=Na, Sn, P, S, Se) in $Na_{11}Sn_2PSe_{12}$ and $Na_{11}Sn_2PS_{12}$, in which $Na_{11}Sn_2PSe_{12}$ has lower bonding energies of Na-Sn and Na-Se.

Cation Substitution/Doping in $Na_{11}Sn_2PS_{12}$. When using Sb^{5+} partial replacement of P^{5+}, a series of $Na_{11+x}Sn_{2+x}(Sb_{1-y}P_y)S_{12}$ conductors are reported with the similar diffraction patterns (**Figure 9c**), which confirms the tetragonal structure and solid solution of Sb/P in structure.[84] In addition, due to the larger radius of Sb^{5+} than P^{5+}, $Na_{11}Sn_2SbS_{12}$ is observed to possess a larger unit cell volume.[127] $Na_{11}Sn_2PnS_{12}$ (Pn=Sb, P) chalcogenide conductors were investigated to compare the Na-ion transport in their crystal structure.[127] Although the Sb replacement of P leads to a larger unit cell volume, the $Na_{11}Sn_2SbS_{12}$ exhibited a lower ionic conductivity of 0.56 mS cm^{-1} than that of $Na_{11}Sn_2PS_{12}$ (1.4 mS cm^{-1}) at RT. The reduced conductivity is due to the different Na site occupancies and the stronger local Na-S bonding to reduce Na^+ ion transport in $Na_{11}Sn_2SbS_{12}$. To understand the P/Sb substitution on structural and conductivity change, a series of $Na_{11+x}Sn_{2+x}(Sb_{1-y}P_y)_{1-x}S_{12}$ conductors were synthesized and studied.[84] In the Sb-rich compounds, adding P leads to a decrease on the unit cell size and thus a simultaneous compression of the Na^+ conduction pathways. **Figure 10d** shows the Nyquist plots of $Na_{11+x}Sn_{2+x}(Sb_{1-y}P_y)_{1-x}S_{12}$ conductors with different ratios of Sb and P (at -60 °C), in which the Sb-rich compound $Na_{11.15}Sn_{2.15}(Sb_{0.75}P_{0.25})_{0.85}S_{12}$ exhibits the smallest grain

resistance and total resistance. In another work, Yao et al. reported that the Se-doping in $Na_{11}Sn_2SbS_{12-x}Se_x$ (x=0.25, 0.5, 0.75) caused the enhancement of RT ionic conductivity and the highest value of 0.66 mS cm^{-1} was achieved for $Na_{11}Sn_2Sb_{11.5}Se_{0.5}$ conductor.[75]

Besides Sb, the aliovalent substitution of P by Group IVA elements (Si, Sn, Ge) also have been investigated.[80] In 2019, a new compound of $Na_{11.25}Sn_{1.5}Si_{0.75}P_{0.75}S_{12}$ was reported to exhibit a RT ionic conductivity of 1.6 mS cm^{-1}.[128] Later, a series of $Na_{11+x}Sn_2P_{1-x}M_xS_{12}$ (M = Ge and Sn) conductors were studied to understand the effects of vacancies concentrations on Na^+ ion transport.[129] They found a reduction of in-grain activation energy for ion transport when Na^+ vacancy concentration was decreased. However, too high vacancy concentration may lead to inefficient Na^+–Na^+ interactions.

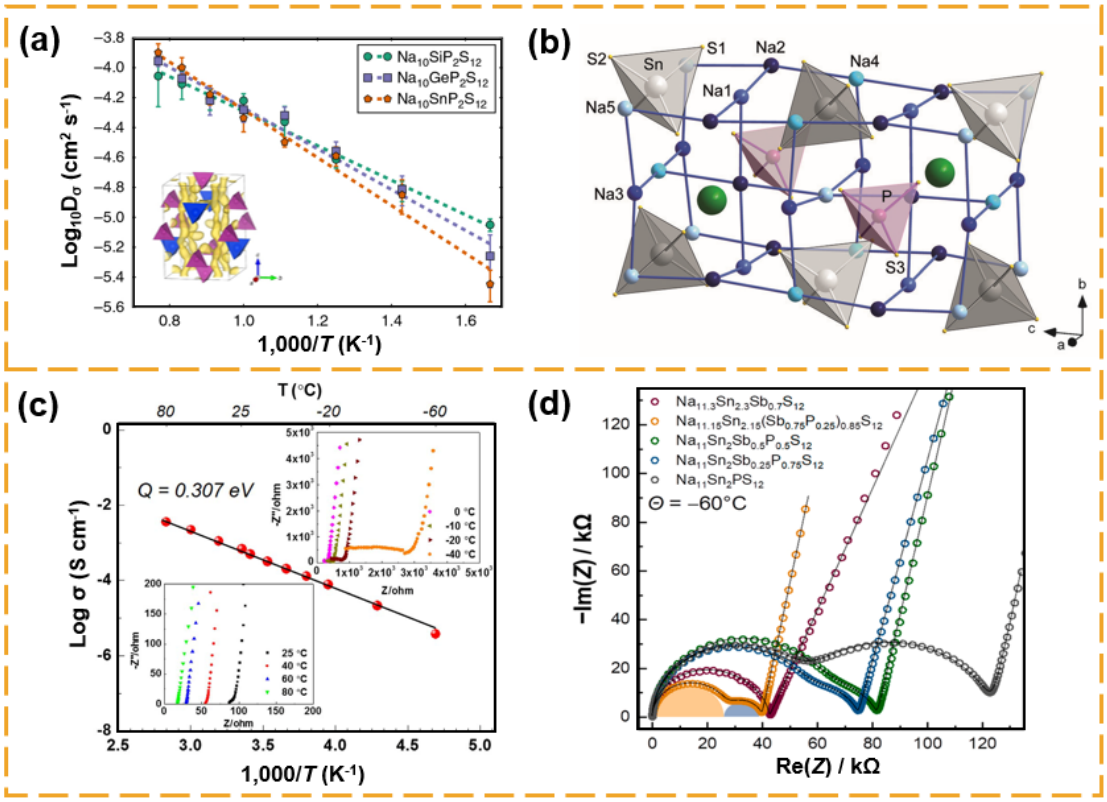

Figure 10. (a) Na-diffusivity in $Na_{10}SiP_2S_{12}$, $Na_{10}GeP_2S_{12}$ and $Na_{10}SnP_2S_{12}$ from AIMD simulation. Inset: Na-ion probability density isosurface (yellow) of $Na_{10}SnP_2S_{12}$ from 600 K AIMD simulation. Reproduced with permission.[124] Copyright 2016, Springer Nature. (b) Illustration of Na-Na interatomic contacts in the crystal structure of $Na_{11}Sn_2PS_{12}$. Large green spheres mark unoccupied vacancies in the NbO-type structure formed by the Na^+ cations. Reproduced with permission.[83] Copyright 2017, Wiley-VCH. (c) Ionic conductivity of $Na_{10.8}Sn_{1.9}PS_{11.8}$. Nyquist plots of the impedance and Arrhenius conductivity plot for

$Na_{10.8}Sn_{1.9}PS_{11.8}$ from −60° to 80°C. Reproduced with permission.[62] Copyright 2018, Elsevier. (d) Nyquist spectra of the complex impedances measured at 213 K (−60 °C) of $Na_{11+x}Sn_{2+x}(Sb_{1-y}P_y)_{1-x}S_{12}$. Reproduced with permission.[84] Copyright 2020, American Chemical Society.

4. Interface between Anode and Sulfide-based Na Conductors

In addition to high ionic conductivity, another critical factor is the interface stability towards electrodes to influence the electrochemical performance of batteries.[131] Sulfide-based solid electrolytes are found to show narrow electrochemical windows indicated based on first principles calculations.[132-134] In specific, the interface compatibility of sulfide SEs to metallic Na anode strongly influence the electrochemical cycling and Na dendrite formation and growth in solid-state Na batteries.

4.1. Interface Studies between Metallic Na Anode and Sulfide Conductors

Na metal is highly chemically reactive; thus, sulfide SEs could decompose when directly contact with the Na metal anode. In 2017, Ceder et al. combined the DFT calculations and experimental analysis to study the thermodynamic stability voltage window of Na_3PCh_4 (Ch=S, Se) model materials. The calculated voltage stability window indicates that Na_3PS_4 can be reduced into Na_2S and other Na-P compounds when the voltage below 1.55 V vs Na/Na^+.[131] The presence of decomposition products of Na_2S and Na_3P at Na/Na_3PS_4 interface was also confirmed by experiments,[135] [136] including *in situ* XPS spectra to reveal the decomposition reaction (Na_3PS_4 + 8 Na→ 4 Na_2S + Na_3P). When using the Na-Sn alloy to replace the Na metal, a relatively stable interface can be obtained due to the decreased interfacial reaction for most sulfides. For example, Na_3PSe_4 SE was found to exhibit a much lower overpotential voltage to Na-Sn than that for Na metal in symmetric cell cycling.[131]

Compared to pure Na_3PS_4, the introduced dopants are considered to influence the interfacial reactions and products. For examples, for t-$Na_{2.9375}PS_{3.9375}Cl_{0.0625}$ SE, NaCl was predicted to appear as one product from the interfacial reactions (**Figure 11a**) by Ong et al.[137] Due to such

"salting" effect, favorable solid electrolyte interphase (SEI) with electronic insulation and ionic conduction were formed, contributing to the enhanced electrochemical stability towards Na metal. Later, a systematic study was performed on the interface between the Na anode and the sulfide SEs (Na_3PS_4, Cl-doped Na_3PS_4, and Na_3SbS_4).[138] The XPS spectra (**Figure 11b**) of cycled Na symmetric cell (Na|SE|Na) clearly revealed the presence of NaCl as well as S-P-Cl compounds at the formed SEI layers in the cases of $Na_{2.9375}PS_{3.9375}Cl_{0.0625}$ and $Na_{2.875}PS_{3.875}Cl_{0.125}$ SEs with Cl-doping, which was found to stabilize the interface by mitigate the decomposition of Na_3PS_4. Moreover, they also reported that the interfacial reaction products at Na_3SbS_4/Na include Na_2S and Na_3Sb in the formed SEI layer. A comprehensive investigation by DFT and AIMD simulations on Na_3PnS_4 and $Na_{11}Tt_2PnS_{12}$ (Pn=P, As, Sb, Tt=Si, Ge, Sn) sulfide conductors was performed by Ong et al.[130] They compared the electrochemical window (EW) for the pristine sulfide and mixed compositions in **Figure 11c**. It is observed that the least electrochemically stable component phase determined the total EW for a mixed composition. In another anion-doping work, Na_3PS_3O with O partial replacement of S was reported to exhibit the improved interface stability due to a slower reaction with Na metal.[139]

The interfacial contact/reaction and interlayer formation can also be facilitated by the stack pressure on the symmetric cells. As shown in **Figure 11d**, the interfacial resistance and total resistance obviously decreases at initially increasing the stack pressure (11-100 MPa) and remains unchanged above 100 MPa.[140] When the Cu | Na_3PS_4 | Na cell was under a constant stack pressure of 45 MPa, the impedance resistance continuously increased over time, reflecting the formation and growth of SEI layer at the interface.

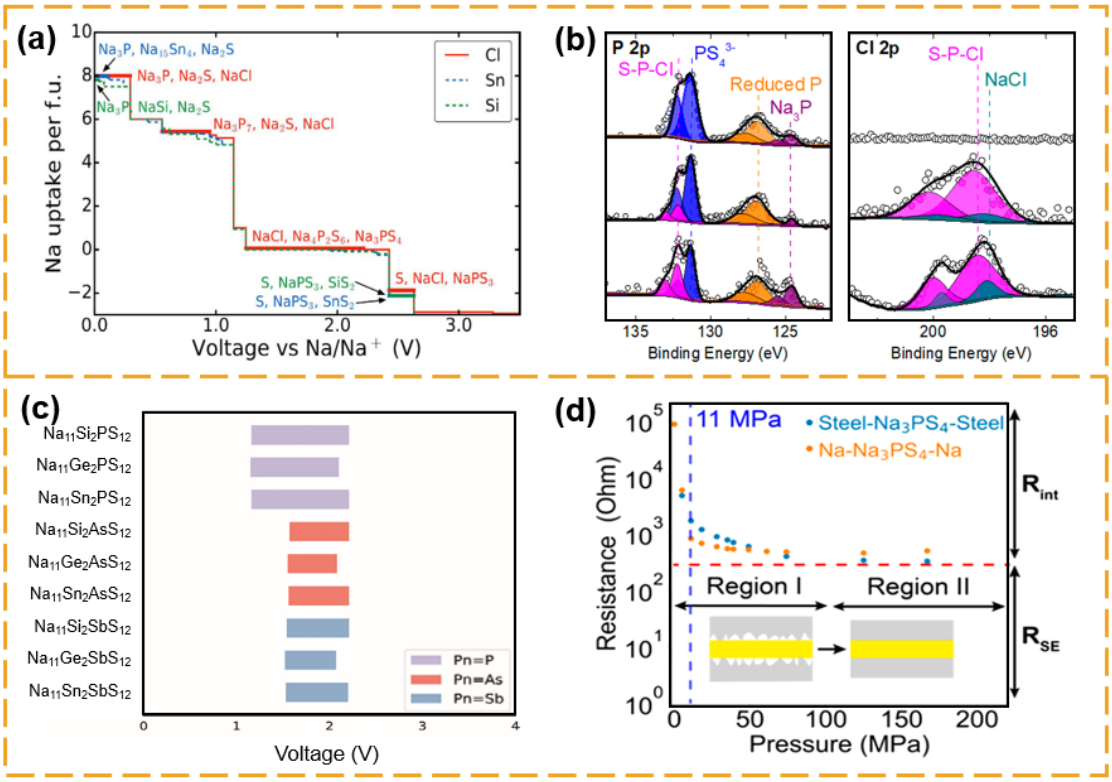

Figure 11. (a) Electrochemical decomposition products of doped Na_3PS_4 compounds (t-$Na_{2.9375}PS_{3.9375}Cl_{0.0625}$ (red solid), c-$Na_{3.0625}Sn_{0.0625}P_{0.9375}S_4$ (blue dashed) and c-$Na_{3.0625}Si_{0.0625}P_{0.9375}S_4$ (green dashed)). Reproduced with permission.[109] Copyright 2016, Springer Nature. (b) XPS spectra (S 2p, P 2p, and Cl 2p region scans) of SSEI after cycling of NPS, 6.25% doped NPSC, and 12.5% doped NPSC. Reproduced with permission.[138] Copyright 2018, American Chemical Society. (c)Electrochemical windows of $Na_{11}Tt_2PnS_{12}$ where Pn = P, As, Sb, and Tt = Si, Ge, Sn. Reproduced with permission.[130] Copyright 2020, Wiley-VCH. (d) Dependence of the M|Na_3PS_4|M (M = Na or steel) cell resistance on the applied stack pressure. Reproduced with permission.[140] Copyright 2020, American Chemical Society.

4.2. Interface Stabilization Strategies between Na Metal and Sulfide Conductors

Due to the intrinsic interfacial reactions between sulfide SEs and Na metal, there are different strategies reported to modify and stabilize the interface: (i) SE treatment, (ii) Na metal treatment, and (iii) additional interlayer.

4.2.1. Treatment on Sulfide-type Conductors

The treatment on SE materials includes (1) doping chemistry and (2) surface passivation. For the doping chemistry, Cl-doped Na_3PS_4 SEs were reported to show enhanced interface stability towards Na metal. Similarly, the solution-process Na_3SbS_4 with Cl-doping exhibited the

improvement on the Na/SE interfacial compatibility.[120] The addition of O-doped $Na_4P_2S_7$ (NaPS) oxysulfide into Na_3SbS_4 was found to contribute to a superior anodic interface.[141] On the other side, the surface treatment was also reported to effectively enhance the interface stability between Na_3SbS_4 and Na metal by espousing the Na_3SbS_4 SE pellet to ambient air to quickly form a thin hydrate phase layer (**Figure 12a**).[142] The decomposition products of hydrate phase caused the change of SEI properties from a mixed conductive interface to a passivating interface.

4.2.2. Modification on Na Metal

Sun et al. deposited an alucone film on Na metal by a molecular layer deposition (MLD) method to stabilize the Na anode and SE interface and limit the decomposition of sulfide SEs (Na_3SbS_4, Na_3PS_4).[143] The sodiated alucone layer is beneficial for Na deposition and dendrite suppression during the electrochemical cycling. Moreover, they also reported the formation of a protective layer of Na_3PS_4 on the surface of Na metal by its reaction with phosphorous sulfide molecules (P_4S_{16}) in a solution-based method.[144] The SEM images of NPS-treated Na foil and bare Na foil after 10 cycles of electrochemical plating/stripping clearly showed the morphology difference after the treatment (**Figure 12b**).

4.2.3. Artificial Interlayer at Interface

As shown in **Figure 12c,** Yao et al. demonstrated to introduce a cellulose−poly(ethylene oxide) (CPEO) interlayer can stabilize the Na/Na_3SbS_4 interface by shutting off the electron pathway of the electrolyte decomposition reaction.[145] They achieved stable Na plating/stripping for 800 cycles at 0.1 mA cm^{-2} in all-solid-state devices at 60 °C. Our group reported another efficient approach by incorporating an ionic liquid electrolyte ((PYR/Na)TFSI) as an interlayer to the Na metal/Na_3SbS_4 interface (**Figure 12d and 12e**) to form a stable and thin SEI to prevent the harmful reactions and inhibit Na dendrites. With such interlayer, the fabricated FeS_2 |Na_3SbS_4 |Na battery delivered a specific capacity of over 300 mA h g^{-1} under the current density of 20

mA g^{-1} at RT.[146] In another work, we introduced a phase-transition polymer electrolyte (PPP/NaTFSI) as an interlayer to stabilize the interface.[147] The phase-transition polymer was in the liquid form above 60 °C and became solid-state at RT. When using TiS_2 as the cathode, the batteries delivered stable cyclability over 300 cycles with remained specific capacity above 100 mA h g^{-1}.

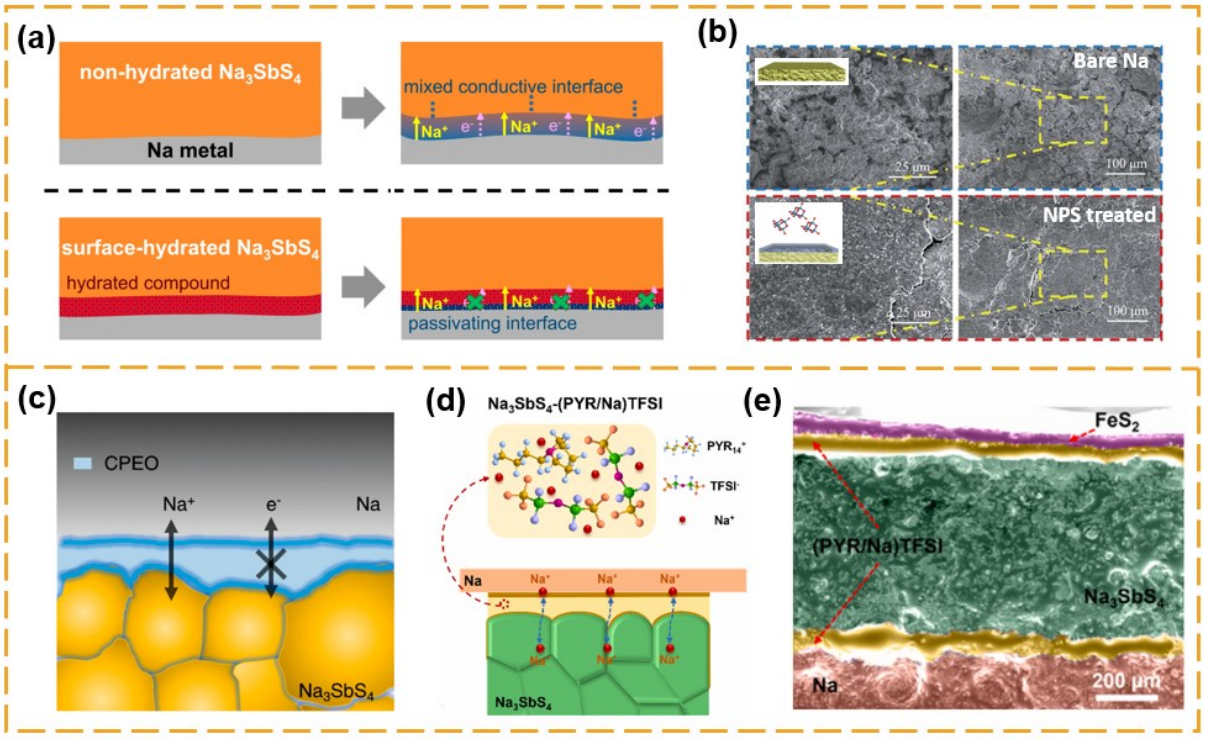

Figure 12. (a)Schematic illustration of solid electrolyte-Na metal interface before (left) and after (right) electrochemical cycling. A mixed conductive interface layer grew upon cycling of the non-hydrated Na_3SbS_4 (top), whereas a passivating interface was formed on the hydrated compound of the surface-hydrated Na_3SbS_4 (bottom); Reproduced with permission.[142] Copyright 2018, Elsevier. (b)Top view SEM image of the bare Na foil and Na@NaPS after 10 cycles of striping/plating. Reproduced with permission.[144] Copyright 2019, Royal Society of Chemistry. (c)Schematic diagram of stable Na-CPEO-Na_3SbS_4 interface. Reproduced with permission.[145] Copyright 2019, American Chemical Society. (d)scheme and (e) cross-sectional SEM image of FeS_2||Na cell with (PYR/Na)TFSI interlayer. Reproduced with permission.[146] Copyright 2022, Elsevier.

5. Composite Cathodes in Solid-state Na Batteries

To achieve high electrochemical performance, the composite cathode should be designed to ensure efficient interface contact, electrochemical/chemical stability as well as reduced stress/strain during cycling.[148] The composite cathode consists of three components: carbon as

electronic conductive additive, sulfide solid electrolyte as the ionic conductive additive, and active cathode material. For sulfide-based solid-state Na batteries (SSNBs), there have been various types of active cathode materials: including transition metal sulfides, sulfur, and oxides, and organic cathodes, which will be reviewed in this session.

5.1. Transition Metal Sulfides as Cathode

Transition metal sulfides such as TiS_2, FeS_2, and Sb_2S_3 have been widely explored in Na-ion batteries.[149], [150] For SSNBs, metal sulfides as cathode show advantages of their moderate potential (1-3 V vs. Na/Na^+), high theoretical specific capacity (300-900 mA h g^{-1}), and more importantly, better compatibility with sulfide SEs compared to oxide counterparts.[151] [152]

5.1.1. Molybdenum Sulfides

Mo_6S_8 is an attractive cathode material due to its small volume change during intercalation and deintercalation process, and the appropriate potential (1.4V vs Na/Na^+). To increase the interface contact between the Mo_6S_8 and Na_3PS_4 SE, Wang et al. demonstrated to use a solution method to coat SE on Mo_6S_8, and then mixed with Na_3PS_4 SE and carbon black to form a designed composite cathode (**Figure 13a**).[148] Due to the intimate contact, the assembled batteries enable to deliver stable cycling up to 500 cycles at 60 °C. In another work, amorphous MoS_x materials with different ratios of Mo to S were explored for SSNBs with $Na_{15}Sn_4$ (anode) and Na_3PS_4 glass-ceramics (SE).[153] In those assembled batteries, the 1st discharge capacities of a-MoS_3, a-MoS_4, a-MoS_5, a-MoS_6, and a-MoS_7 were 260, 420, 600, 690, and 770 mA h g^{-1}, respectively, which correspond to reactions with 1.9, 3.5, 5.7, 7.4, and 9.2 molar equivalents of Na. However, a-MoS_6 showed the highest reversible capacity of 540 mA h g^{-1} among all compositions. Similarly, using Na_3PS_4 as the SE and Na-Sn as the anode, the exfoliated MoS_2 nanosheet was also demonstrated as the active material in the composite cathode (MoS_2-Na_3PS_4-carbon).[151] When cycled at 60 °C, the SSNBs showed the discharge capacity reached 373 mA h g^{-1} and remained reversible capacity of 269 mA h g^{-1} after 100 cycles.

5.1.2. Titanium Sulfides

In SSNBs, TiS_2 has been demonstrated as cathode with several sulfide SEs due to its structure stability and reversibility.[59, 61, 106, 147] Yao et al. fabricated TiS_2/Na batteries using $Na_{11}Sn_2PS_{12}$ SE that synthesized from two approaches (liquid-based and ball-milling). It was found that the SSNBs with liquid-synthesized $Na_{11}Sn_2PS_{12}$ delivered great discharge capacity of 231 mA h g^{-1} and better reversible capacity retention (142.4 mA h g^{-1} vs 110.5 mA h g^{-1} for ball-milled sample) after 10 cycles. The better capacity remaining is due to the fine particle size in liquid synthesized $Na_{11}Sn_2PS_{12}$ electrolyte, which has better physical contact at interface to reduce the interfacial resistance. In another work using $Na_{11}Sn_2PSe_{12}$ as SE and cycle voltage of 1.5-2.5 V, the TiS_2 cathode delivered a lower specific capacity of 85 mA h g^{-1}, but it was stably cycled for 100 cycles.[61] To increase the capacity, TiS_3 sulfide (synthesized via ball milling of TiS_2 and S) was used as active material in the composite cathode (TiS_3-NPS-Carbon).[154] Although the 1st discharge capacity of over 300 mA h g^{-1} was obtained at 25 °C, the capacity decayed dramatically after 10th cycles due to the aggregation of TiS_3 particles after cycling.

5.1.3. Iron Sulfides

The core-shell structured $Fe_{1-x}S@Na_{2.9}PS_{3.95}Se_{0.05}$ composite cathode was prepared by liquid coating a SE layer on $Fe_{1-x}S$ nanorod.[152] The element mapping via STEM-EDS confirmed the homogeneous distribution of Fe, S, Na, P, and Se in the nanocomposite cathode. With such nanostructure designed cathode, the assembled SSNBs delivered a high specific capacity and excellent rate capacity at RT. In specific, the reversible discharge capacities of 899.2, 795.5, 655.1, 437.9, and 300.4 mA h g^{-1} at current densities of 20, 50, 100, 150, and 200 mA g^{-1}, respectively. In another work, cobalt-doped $Co_xFe_{1-x}S_2$ was demonstrated in SSNBs by using bi-layer of $Na_{11}Sn_2SbS_{11.5}Se_{0.5}$ and Na_3PS_4 SEs.[75] The highest initial capacity of 674.3 mA h g^{-1} was obtained for $Co_{0.1}Fe_{0.9}S_2$ at a current density of 50 mA g^{-1}.

5.2 Sulfur Cathode

Sulfur materials such as S and Na_2S are facing main challenges of poor electrical conductivity and a large volume change during charging/discharging. Thus, mixing sulfide SE with carbon and sulfur can facilitate ion/electron transport and promote the electrochemical reaction of sulfur cathodes. As demonstrated in Na-ion batteries, adding and engineering carbon into cathode composite is important to increase its electrical conductivity and promote the electrochemical kinetics.[155], [156]

Selenium-doped sulfurized polyacrylonitrile (Se_xS_{1-x}@PAN) was reported as the cathode in the RT solid-state Na-S batteries.[136, 141, 157] Xie et al. prepared Se_xS_{1-x}@PAN composite cathode ($Se_{0.05}S_{0.95}$:Na_3PS_4:carbon ratio of 2:6:2) to boost the electronic and ionic conductivities of S cathode.[136] With pairing with the Na-Sn anode (treated by Pyr14FSI to form *in situ* SEI), the cell with $Se_{0.05}S_{0.95}$@PAN cathode displayed higher reversible capacities than that with S@PAN cathode for all C-rates (**Figure 13b**), for instance, 717.3 mA h g^{-1} vs 574.1 mA h g^{-1} for 0.1 C rate. In another work, Zhang et al. designed Na_3SbS_4 coating on SeS-PAN cathode to achieve a lower resistance than the cathode composite prepared by the mixing method.[157] The fabricated batteries delivered a reversible capacity of 504 mA h g^{-1} and a capacity retention of 98.9% for 100 cycles at a current density of 437.4 mA g^{-1}. Later, they adopted the optimal cathode $Se_{0.8}S_{7.2}$@PAN and oxysulfide glass (NaPSO-Na_3SbS_4) to achieve long cycling stability of 1000 cycles.[141]

Instead of S, nanosized Na_2S has been employed to prepare Na_2S-Na_3PS_4-carbon nanocomposite cathode and cycled between the voltage window of 0.5-3.0 V.[158] SEM and TEM (**Figure 13c**) confirmed that each component was homogeneously distributed in the nanocomposite cathode. The nanosized particles in cathode achieved sufficient contact at interface and high conductivity, resulting in a reversible capacity of 869.2 mA h g^{-1} and

remained 438.4 mA h g^{-1} after 50 cycles at 50 mA g^{-1} at 60 °C in the solid-state Na-S batteries. Later, they employed a casting-annealing process to achieve better interface contacts in Na_2S-Na_3PS_4-carbon composite cathode,[159] which enabled to assemble solid-state Na-S batteries to deliver a reversible capacity of 810 mA h g^{-1} for 50 cycles (50 mA g^{-1} and 60 °C).

Taking the S-Na_3PS_4-carbon cathode as example, two types of preparation approaches (hand-mixed electrode and mechanically milled electrode) were compared.[160] **Figure 13d** showed that the mechanically milled electrode delivered much higher capacity of 1,112 mA h g^{-1} than that prepared by hand mixing (51 mA h g^{-1}) due to better solid/solid interface contact to reduce the diffusion resistance in the milled cathode. In addition to Na_3PS_4 SE, P_2S_5 is also used as the ion-conductive component in the composite electrode. The SSNBs composite cathode of S-carbon-P_2S_5 showed a high reversible specific capacity of 680 mA h g^{-1}, much higher than the battery with S-Na_3PS_4 cathode.[161]

To increase the conductivity of S-based composite cathode, S-Na_3SbS_4-C nanocomposite cathode was prepared by a combination of liquid-phase reaction and ball milling to create the nanoscale electronic/ionic pathways.[162] HRTEM image showed the lattice fringes from super P carbon, S and Na_3SbS_4, respectively. The fabricated S- Na_3SbS_4-C/Na cells successfully delivered an initial capacity of 1504.3 mA h g^{-1} at 50mA g^{-1} with a Coulombic efficiency of 98.5% at RT as well as excellent rate performance (capacity of 771.2 mA h g^{-1} at the current density of 1000 mA g^{-1}). Another strategy for S-Na_3SbS_4-C composite preparation was to fill the carbon micropores with sulfur and Na_3SbS_4 by a combination of liquid-phase mixing and ball milling.[163] The SSNBs with the cathode design showed a high initial discharge capacity of 1560 mA h g^{-1} (0.064 mA cm^{-2} and 25 °C) retained and 93% capacity after 50 cycles, due to good interface between the S-C and Na_3SbS_4 in cathode composite.

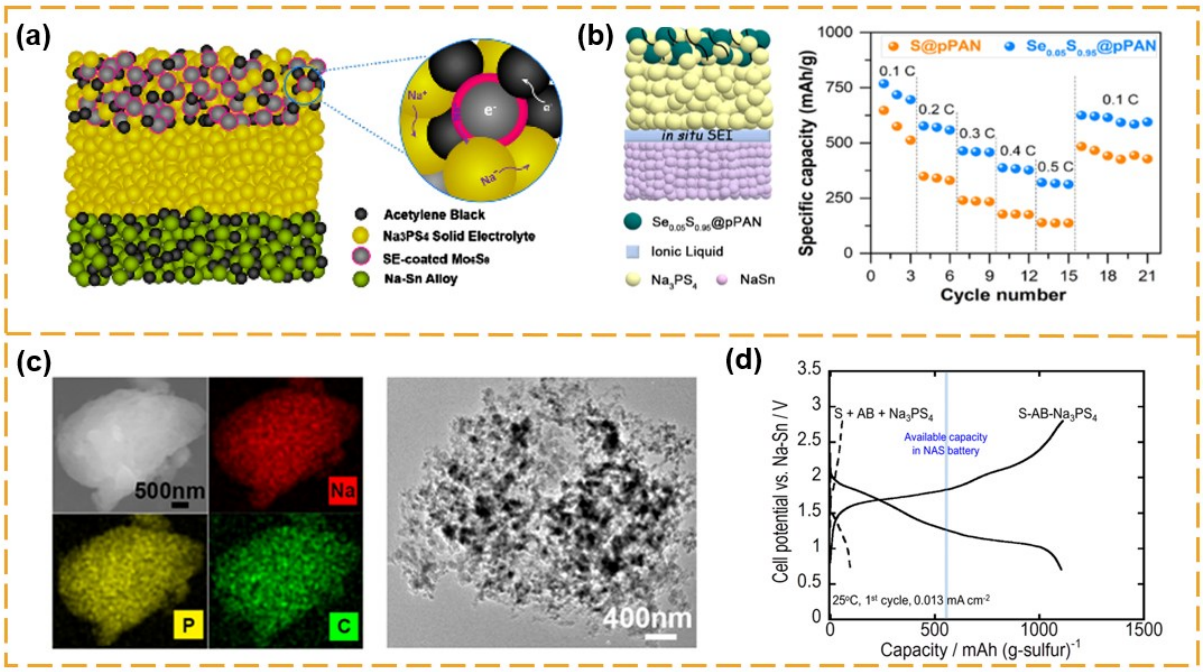

Figure 13. (a) Schematic diagram of a bulk-type ASIB enabled by a SE-coated Mo_6S_8 cathode; Reproduced with permission.[148] Copyright 2018, American Chemical Society. (b) Schematic of $Se_{0.08}S_{0.95}$@pPAN|NPS|NaSn battery structure with the IL modification, and comparison of rate performance of S@pPAN and $Se_{0.05}S_{0.95}$@pPAN in a solid-state battery operated at RT (1C= 1500 mA h g^{-1}). Reproduced with permission.[136] Copyright 2020, American Chemical Society. (c) SEM image and elemental mappings of sodium, phosphorus, and carbon as well as TEM image for the NPS-nano-Na_2S−C nanocomposite cathode. Reproduced with permission.[158] Copyright 2017, American Chemical Society. (d) Discharge−charge curves at the first cycle of the all-solid-state sodium cells using the sulfur composite electrodes prepared by hand mixing (S+AB+Na_3PS_4) or mechanical milling (S−AB−Na_3PS_4). Reproduced with permission.[160] Copyright 2017, American Chemical Society.

5.3 Oxide Cathode

Oxide cathodes such as $NaCrO_2$, $NaCoO_2$ and $Na_3V_2(PO_4)_3$ have been studied when pairing with sulfide SEs for SSNBs. However, most of batteries exhibit fast capacity decay due to their chemical/electrochemical instability at the interface. For instance, first-principles calculations predicted the formation of PO_4^{3-} at the interface of $NaCoO_2$/Na_3PS_4.[164] To reduce such interfacial reactions, the design cathode structure and compositions is needed.

The Na-Sn/Na_3PS_4/$NaCrO_2$ cell was reported to show cycling for 15 cycles with initial discharge capacity of 130 mA g^{-1} when cycling within the electrochemical window of 1.2-4.0V.[67] Later, they demonstrated amorphous oxide cathodes of $Na_{0.7}CoO_2$-Na_xMO_y (M=N, S,

P, B or C) and fabricated SSNBs with Na_3PS_4 as SE and Na-Sn as the anode.[165] For the composite cathode of $Na_{0.76}Co_{0.8}N_{0.2}O_{2.2}$-$Na_3PS_4$, the cell delivered a capacity of 170 mA h g^{-1} for the 15th cycle discharge (**Figure 14a**) thanks to the amorphous structure (**Figure 14b)**. In addition, SSNBs with $Na_3V_2(PO_4)_3$ cathode, $Na_3PS_{3.8}Cl_{0.2}$ SE and Na anode had been reported to show an initial capacity of 100 mA g^{-1}.[47] Solid-state Na-ion batteries with $Na_{2+2\delta}Fe_{2-\delta}(SO_4)_3$ as the cathode and $Na_2Ti_3O_7$ as the anode were also explored to pair with the Sn-doped Na_3PS_4 as the SE.[105] For Na_3SbS_4 SE, Jung et al. reported to prepare a thin SE coating on $NaCrO_2$ particle surface to obtain great interface contact (**Figure 14c**).[52] The NCO/Na-Sn cell with the coated cathode displayed much higher specific capacity that of the mixed electrode.

5.4 Organic Cathode

Organic carbonyl compounds are also promising cathode materials due to the sustainable resources and controllable molecular design.[166, 167] In 2018, Yao et al. first demonstrated $Na_4C_6O_6$ that is (electro) chemical compatible with Na_3PS_4 SE.[166] When paring with $Na_{15}Sn_4$ anode (**Figure 14d and e**), the SSNBs delivered a reversible capacity of 182 mA h g^{-1} (90% of the theoretical capacity), and remained at a capacity of 140 mA h g^{-1} after 100 cycles at 0.1 C. Later, the same group demonstrated another quinone, pyrene-4,5,9,10-tetraone (PTO) with higher theoretical specific capacity of 409 mA h g^{-1} and a higher working potential of 2.2 V (versus Na^+/Na).[167] The fabricated batteries exhibited a capacity of 322 mA h g^{-1} at 0.1 C and 280 mA h g^{-1} at 0.3 C, and remained at 89% capacity retention after 500 cycles at 0.3 C (**Figure 14f**).

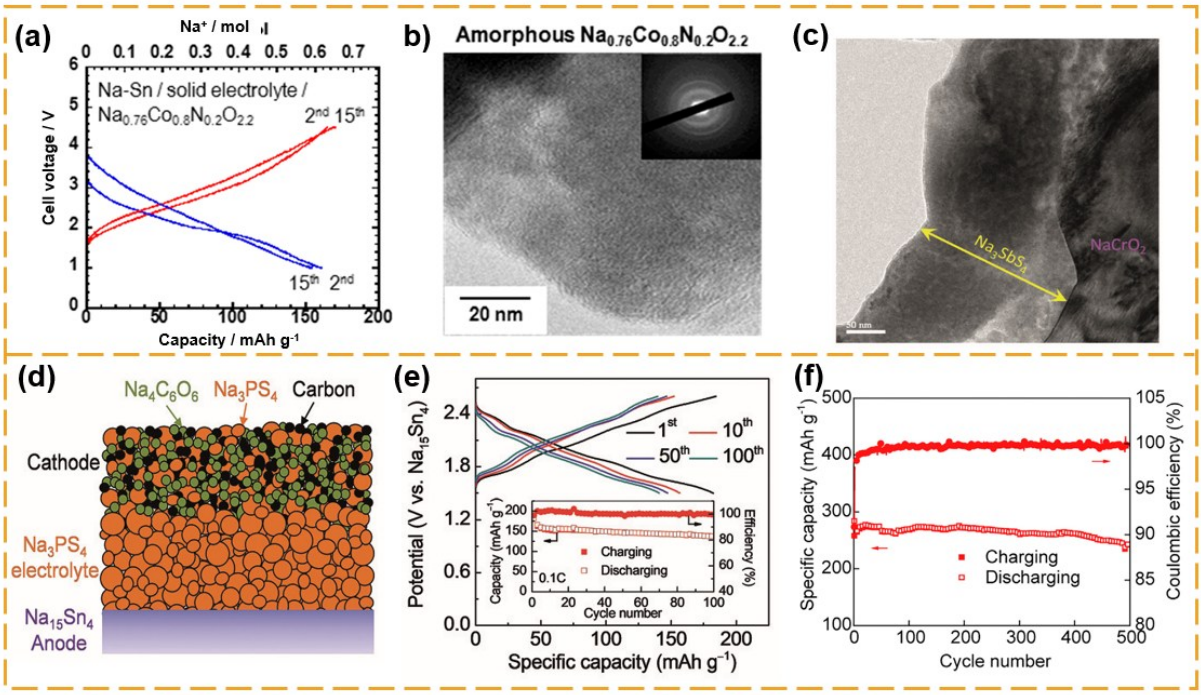

Figure 14. (a) Charge−discharge curves for the cell prepared using a composite electrode of $Na_{0.76}Co_{0.8}N_{0.2}O_{2.2}$ in the voltage range of 1.0−4.5 V, and (b) HTEM image and electron diffraction pattern of the milled $Na_{0.76}Co_{0.8}N_{0.2}O_{2.2}$. Reproduced with permission.[165] Copyright 2018, American Chemical Society. (c) HRTEM image of FIB-sectioned Na_3SbS_4-coated $NaCrO_2$. Reproduced with permission.[168] Copyright 2016, Wiley-VCH. (d)Schematic diagram of the $Na_4C_6O_6|Na_3PS_4|Na_{15}Sn_4$ ASSSB, (e) charge/discharge voltage profiles at different cycle numbers at 0.1 C at 60 C (Inset: Capacity and coulombic efficiency versus cycle number at 0.1 C). Reproduced with permission.[166] Copyright 2017, Wiley-VCH. (f) The capacity and Coulombic efficiency versus cycle number for PTO-NR-based cell at 0.3 C. Reproduced with permission.[167] Copyright 2019, Elsevier.

6. Conclusions and Outlook

This review systemically summarizes the recent progress on the synthesis, structure, and conductivity of three representative (Na_3PS_4, Na_3SbS_4 and $Na_{11}Sn_2PS_{12}$) sulfide-based superionic conductors. Additionally, the interface stability of these SEs toward the Na anode and interface modification strategies, as well as the solid-state batteries pairing with various types of cathodes materials (i.e., Sulfur, MS_x, oxides and organics) are discussed. In general, sulfide-based Na-ion conductors have many advantages such as high ionic conductivity, low-cost materials and flexible compositions, densification by cold-pressing. Nevertheless, they are facing challenges, including moisture/air sensitivity and chemical/electrochemical instability to

high voltage oxide cathode, etc. In addition, as a solid-state battery is a complicated system, thus achieving excellent battery performance relies on many factors beyond only the solid electrolyte itself, which include, for instance, the matched electrode materials and the optimized electrode/SE interface.

While there is still a long way to go to realize complete applications of sulfide-based solid-state Na batteries, there are many significant ongoing research and development in this field, and we can expect continued progress and breakthroughs in the coming years. Regarding the future research, we propose the following prospects:

Advanced materials design and synthesis. Experiments and theoretical simulation should be combined to explore novel SE materials with optimal doping chemistry to meet the requirements on both high ionic conductivity and great electrochemical stability. Current doping chemistry in SEs sometimes increases the Na-ion conductivity by sacrificing the stability. Specifically, the optimal material design to overcome that trade-off is needed.

Engineering interfaces of SE/electrode and within composite cathode. These two types of interfaces both require intimate contact and minimum solid/solid resistance, not only at the battery assembly, but also after repeated battery cycling. However, they have different requirements on conductive behaviors. At the pellet interface (SE/electrode), the formed SEI layer should be ionically conductive but electronically insulating, while the composite cathodes are expected to have mixed ionic and electronic conductivity. Thus, different interface engineering strategies should be developed.

In situ/operando characterizations on SEI at interface and electrode materials. Advanced characterization tools to study the interface instability under the electrochemical environment are necessary. Fundamental understanding of the degradation mechanism, *in situ* SEI formation, interfacial reaction, as well as stress/strain distribution and evolution are important for materials and interface design to achieve high performance batteries.

Establish standards and protocols for conductivity tests and battery assembly/cycling. For a SE with the same composition, its conductivity is strongly influenced by the processing parameters (e.g. sintering, applied pressure), measurement conditions (e.g., block electrode, external pressure). Also using the same SE, the battery cycling performance is also closely related to the battery assembly (cell type, applied pressure).

Acknowledgements

The authors thank the support from U.S. National Science Foundation under awards No. 2047460 and Department of Energy (DOE) Office of Basic Energy Science (BES) under award SC-0021257.

Received: ((will be filled in by the editorial staff))
Revised: ((will be filled in by the editorial staff))
Published online: ((will be filled in by the editorial staff))

References

1. Braga, M. H.; Grundish, N. S.; Murchison, A. J.; Goodenough, J. B., *Energy & Environmental Science* **2017,** *10* (1), 331-336. DOI 10.1039/c6ee02888h.
2. Li, J.; Ma, C.; Chi, M.; Liang, C.; Dudney, N. J., *Advanced Energy Materials* **2015,** *5* (4), 1401408. DOI 10.1002/aenm.201401408.
3. Janek, J.; Zeier, W. G., *Nature Energy* **2016,** *1* (9), 16141. DOI 10.1038/nenergy.2016.141.
4. Kato, Y.; Hori, S.; Saito, T.; Suzuki, K.; Hirayama, M.; Mitsui, A.; Yonemura, M.; Iba, H.; Kanno, R., *Nature Energy* **2016,** *1* (4), 16030. DOI 10.1038/nenergy.2016.30.
5. Ellis, B. L.; Nazar, L. F., *Current Opinion in Solid State and Materials Science* **2012,** *16* (4), 168-177. DOI 10.1016/j.cossms.2012.04.002.
6. Zhou, W.; Li, Y.; Xin, S.; Goodenough, J. B., *ACS Cent Sci* **2017,** *3* (1), 52-57. DOI 10.1021/acscentsci.6b00321.
7. Zhao, Y.; Adair, K. R.; Sun, X., *Energy & Environmental Science* **2018,** *11* (10), 2673-2695. DOI 10.1039/C8EE01373J.
8. Zhao, C.; Liu, L.; Qi, X.; Lu, Y.; Wu, F.; Zhao, J.; Yu, Y.; Hu, Y.-S.; Chen, L., *Advanced Energy Materials* **2018,** *8* (17), 1703012. DOI 10.1002/aenm.201703012.
9. Bachman, J. C.; Muy, S.; Grimaud, A.; Chang, H. H.; Pour, N.; Lux, S. F.; Paschos, O.; Maglia, F.; Lupart, S.; Lamp, P.; Giordano, L.; Shao-Horn, Y., *Chem Rev* **2016,** *116* (1), 140-62. DOI 10.1021/acs.chemrev.5b00563.
10. Lu, Y.; Li, L.; Zhang, Q.; Niu, Z.; Chen, J., *Joule* **2018,** *2* (9), 1747-1770. DOI https://doi.org/10.1016/j.joule.2018.07.028.
11. Hwang, J.-Y.; Myung, S.-T.; Sun, Y.-K., *Chemical Society Reviews* **2017,** *46* (12), 3529-3614. DOI 10.1039/C6CS00776G.
12. Dustmann, C.-H., *Journal of Power Sources* **2004,** *127* (1), 85-92. DOI https://doi.org/10.1016/j.jpowsour.2003.09.039.

13. Takahashi, T.; Kuwabara, K.; Shibata, M., *Solid State Ionics* **1980,** *1* (3), 163-175. DOI https://doi.org/10.1016/0167-2738(80)90001-6.
14. Kimpa, M. I.; Mayzan, M. Z. H.; Yabagi, J. A.; Nmaya, M. M.; Isah, K. U.; Agam, M. A., *IOP Conference Series: Earth and Environmental Science* **2018,** *140*. DOI 10.1088/1755-1315/140/1/012156.
15. Liu, T. F.; Wang, B.; Gu, X. X.; Wang, L.; Ling, M.; Liu, G.; Wang, D. L.; Zhang, S. Q., *Nano Energy* **2016,** *30*, 756-761. DOI 10.1016/j.nanoen.2016.09.024.
16. Hayashi, A.; Noi, K.; Sakuda, A.; Tatsumisago, M., *Nat Commun* **2012,** *3*, 856. DOI 10.1038/ncomms1843.
17. Tatsumisago, M.; Hayashi, A., *International Journal of Applied Glass Science* **2014,** *5* (3), 226-235. DOI 10.1111/ijag.12084.
18. Wang, H.; Chen, Y.; Hood, Z. D.; Sahu, G.; Pandian, A. S.; Keum, J. K.; An, K.; Liang, C., *Angewandte Chemie International Edition* **2016,** *55* (30), 8551-8555. DOI 10.1002/anie.201601546.
19. Schlem, R.; Banik, A.; Eckardt, M.; Zobel, M.; Zeier, W. G., *ACS Applied Energy Materials* **2020,** *3* (10), 10164-10173. DOI 10.1021/acsaem.0c01870.
20. Kwak, H.; Lyoo, J.; Park, J.; Han, Y.; Asakura, R.; Remhof, A.; Battaglia, C.; Kim, H.; Hong, S.-T.; Jung, Y. S., *Energy Storage Materials* **2021,** *37*, 47-54. DOI https://doi.org/10.1016/j.ensm.2021.01.026.
21. Cuan, J.; Zhou, Y.; Zhou, T.; Ling, S.; Rui, K.; Guo, Z.; Liu, H.; Yu, X., *Advanced Materials* **2019,** *31* (1), 1803533. DOI https://doi.org/10.1002/adma.201803533.
22. Luo, X.; Rawal, A.; Salman, M. S.; Aguey-Zinsou, K.-F., *ACS Applied Nano Materials* **2022,** *5* (1), 373-379. DOI 10.1021/acsanm.1c03187.
23. Hueso, K. B.; Armand, M.; Rojo, T., *Energy & Environmental Science* **2013,** *6* (3), 734-749. DOI 10.1039/C3EE24086J.
24. Lu, X.; Xia, G.; Lemmon, J. P.; Yang, Z., *Journal of Power Sources* **2010,** *195* (9), 2431-2442. DOI https://doi.org/10.1016/j.jpowsour.2009.11.120.
25. Park, K. H.; Bai, Q.; Kim, D. H.; Oh, D. Y.; Zhu, Y.; Mo, Y.; Jung, Y. S., *Advanced Energy Materials* **2018,** *8* (18), 1800035. DOI 10.1002/aenm.201800035.
26. Hayashi, A.; Sakuda, A.; Tatsumisago, M., *Frontiers in Energy Research* **2016,** *4*. DOI 10.3389/fenrg.2016.00025.
27. Sakuda, A.; Hayashi, A.; Tatsumisago, M., *Sci. Rep.* **2013,** *3*, 2261. DOI 10.1038/srep02261.
28. Zhang, Q.; Cao, D.; Ma, Y.; Natan, A.; Aurora, P.; Zhu, H., *Advanced Materials* **2019,** *31* (44), 1901131. DOI 10.1002/adma.201901131.
29. Jung, Y. S.; Oh, D. Y.; Nam, Y. J.; Park, K. H., *Israel Journal of Chemistry* **2015,** *55* (5), 472-485. DOI 10.1002/ijch.201400112.
30. Richards, W. D.; Miara, L. J.; Wang, Y.; Kim, J. C.; Ceder, G., *Chemistry of Materials* **2016,** *28* (1), 266-273. DOI 10.1021/acs.chemmater.5b04082.
31. Kim, K. J.; Balaish, M.; Wadaguchi, M.; Kong, L.; Rupp, J. L. M., *Advanced Energy Materials* **2021,** *11* (1), 2002689. DOI https://doi.org/10.1002/aenm.202002689.
32. Tatsumisago, M.; Nagao, M.; Hayashi, A., *Journal of Asian Ceramic Societies* **2018,** *1* (1), 17-25. DOI 10.1016/j.jascer.2013.03.005.
33. Li, X.; Liang, J.; Yang, X.; Adair, K. R.; Wang, C.; Zhao, F.; Sun, X., *Energy & Environmental Science* **2020,** *13* (5), 1429-1461. DOI 10.1039/C9EE03828K.
34. Wang, C.; Fu, K.; Kammampata, S. P.; McOwen, D. W.; Samson, A. J.; Zhang, L.; Hitz, G. T.; Nolan, A. M.; Wachsman, E. D.; Mo, Y.; Thangadurai, V.; Hu, L., *Chemical Reviews* **2020,** *120* (10), 4257-4300. DOI 10.1021/acs.chemrev.9b00427.
35. Hayashi, A.; Noi, K.; Sakuda, A.; Tatsumisago, M., *Nature Communications* **2012,** *3* (1), 856. DOI 10.1038/ncomms1843.

36. Jia, H.; Sun, Y.; Zhang, Z.; Peng, L.; An, T.; Xie, J., *Energy Storage Materials* **2019,** *23*, 508-513. DOI https://doi.org/10.1016/j.ensm.2019.04.011.
37. Nasu, A.; Inaoka, T.; Tsuji, F.; Motohashi, K.; Sakuda, A.; Tatsumisago, M.; Hayashi, A., *ACS Applied Materials & Interfaces* **2022,** *14* (21), 24480-24485. DOI 10.1021/acsami.2c05090.
38. Zhou, L.; Bazak, J. D.; Singh, B.; Li, C.; Assoud, A.; Washton, N. M.; Murugesan, V.; Nazar, L. F., *Angewandte Chemie International Edition* **2023,** *62* (30), e202300404. DOI https://doi.org/10.1002/anie.202300404.
39. Hayashi, A.; Noi, K.; Tanibata, N.; Nagao, M.; Tatsumisago, M., *Journal of Power Sources* **2014,** *258*, 420-423. DOI 10.1016/j.jpowsour.2014.02.054.
40. Tanibata, N.; Noi, K.; Hayashi, A.; Tatsumisago, M., *RSC Adv.* **2014,** *4* (33), 17120-17123. DOI 10.1039/c4ra00996g.
41. Hibi, Y.; Tanibata, N.; Hayashi, A.; Tatsumisago, M., *Solid State Ionics* **2015,** *270*, 6-9. DOI 10.1016/j.ssi.2014.11.024.
42. Chu, I.-H.; Kompella, C. S.; Nguyen, H.; Zhu, Z.; Hy, S.; Deng, Z.; Meng, Y. S.; Ong, S. P., *Sci. Rep.* **2016,** *6*, 33733. DOI 10.1038/srep33733

https://www.nature.com/articles/srep33733#supplementary-information.
43. Bo, S.-H.; Wang, Y.; Ceder, G., *Journal of Materials Chemistry A* **2016,** *4* (23), 9044-9053. DOI 10.1039/c6ta03027k.
44. Moon, C. K.; Lee, H.-J.; Park, K. H.; Kwak, H.; Heo, J. W.; Choi, K.; Yang, H.; Kim, M.-S.; Hong, S.-T.; Lee, J. H.; Jung, Y. S., *ACS Energy Letters* **2018,** *3* (10), 2504-2512. DOI 10.1021/acsenergylett.8b01479.
45. Tanibata, N.; Noi, K.; Hayashi, A.; Tatsumisago, M., *Solid State Ionics* **2018,** *320*, 193-198. DOI https://doi.org/10.1016/j.ssi.2018.02.042.
46. Takeuchi, S.; Suzuki, K.; Hirayama, M.; Kanno, R., *Journal of Solid State Chemistry* **2018,** *265*, 353-358. DOI https://doi.org/10.1016/j.jssc.2018.06.023.
47. Feng, X.; Chien, P.-H.; Zhu, Z.; Chu, I.-H.; Wang, P.; Immediato-Scuotto, M.; Arabzadeh, H.; Ong, S. P.; Hu, Y.-Y., *Advanced Functional Materials* **2019,** *29* (9), 1807951. DOI 10.1002/adfm.201807951.
48. Atsunori, M.; Hirotada, G.; Phuc, N. H. H., *Heliyon* **2019,** *5* (11), e02760. DOI 10.1016/j.heliyon.2019.e02760.
49. Hayashi, A.; Masuzawa, N.; Yubuchi, S.; Tsuji, F.; Hotehama, C.; Sakuda, A.; Tatsumisago, M., *Nature Communications* **2019,** *10* (1), 5266. DOI 10.1038/s41467-019-13178-2.
50. Chi, X.; Zhang, Y.; Hao, F.; Kmiec, S.; Dong, H.; Xu, R.; Zhao, K.; Ai, Q.; Terlier, T.; Wang, L.; Zhao, L.; Guo, L.; Lou, J.; Xin, H. L.; Martin, S. W.; Yao, Y., *Nature Communications* **2022,** *13* (1), 2854. DOI 10.1038/s41467-022-30517-y.
51. Long Zhang , D. Z., Kun Yang , Xinlin Yan , Limin Wang , Jianli Mi , Bo Xu , and Yueming Li, *advanced science* **2016,** *3*, 1600089.
52. Banerjee, A.; Park, K. H.; Heo, J. W.; Nam, Y. J.; Moon, C. K.; Oh, S. M.; Hong, S. T.; Jung, Y. S., *Angew Chem Int Ed Engl* **2016,** *55* (33), 9634-8. DOI 10.1002/anie.201604158.
53. Park, K. H.; Kim, D. H.; Kwak, H.; Jung, S. H.; Lee, H.-J.; Banerjee, A.; Lee, J. H.; Jung, Y. S., *Journal of Materials Chemistry A* **2018,** *6* (35), 17192-17200. DOI 10.1039/C8TA05537H.
54. Kim, T. W.; Park, K. H.; Choi, Y. E.; Lee, J. Y.; Jung, Y. S., *Journal of Materials Chemistry A* **2018,** *6* (3), 840-844. DOI 10.1039/c7ta09242c.
55. Yubuchi, S.; Ito, A.; Masuzawa, N.; Sakuda, A.; Hayashi, A.; Tatsumisago, M., *Journal of Materials Chemistry A* **2020,** *8* (4), 1947-1954. DOI 10.1039/C9TA02246E.
56. Gamo, H.; Phuc, N. H. H.; Muto, H.; Matsuda, A., *ACS Applied Energy Materials* **2021,** *4* (6), 6125-6134. DOI 10.1021/acsaem.1c00927.

57. Feng, X.; Fang, H.; Liu, P.; Wu, N.; Self, E. C.; Yin, L.; Wang, P.; Li, X.; Jena, P.; Nanda, J.; Mitlin, D., *Angewandte Chemie International Edition* **2021,** *60* (50), 26158-26166. DOI https://doi.org/10.1002/anie.202110699.
58. Zhang, Z.; Ramos, E.; Lalère, F.; Assoud, A.; Kaup, K.; Hartman, P.; Nazar, L. F., *Energy & Environmental Science* **2018,** *11* (1), 87-93. DOI 10.1039/C7EE03083E.
59. Weng, W.; Wan, H.; Liu, G.; Wu, L.; Wu, J.; Yao, X., *ACS Applied Energy Materials* **2021,** *4* (2), 1467-1473. DOI 10.1021/acsaem.0c02671.
60. Richards, W. D.; Tsujimura, T.; Miara, L. J.; Wang, Y.; Kim, J. C.; Ong, S. P.; Uechi, I.; Suzuki, N.; Ceder, G., *Nat Commun* **2016,** *7*, 11009. DOI 10.1038/ncomms11009.
61. Yu, Z.; Shang, S.-L.; Wang, D.; Li, Y. C.; Yennawar, H. P.; Li, G.; Huang, H.-T.; Gao, Y.; Mallouk, T. E.; Liu, Z.-K.; Wang, D., *Energy Storage Materials* **2019,** *17*, 70-77. DOI 10.1016/j.ensm.2018.11.027.
62. Yu, Z.; Shang, S.-L.; Gao, Y.; Wang, D.; Li, X.; Liu, Z.-K.; Wang, D., *Nano Energy* **2018,** *47*, 325-330. DOI https://doi.org/10.1016/j.nanoen.2018.01.046.
63. Weng, W.; Liu, G.; Shen, L.; Yao, X., *Journal of Power Sources* **2021,** *512*, 230485. DOI https://doi.org/10.1016/j.jpowsour.2021.230485.
64. Wang, H.; Chen, Y.; Hood, Z. D.; Sahu, G.; Pandian, A. S.; Keum, J. K.; An, K.; Liang, C., *Angew. Chem. Int. Ed.* **2016,** *55* (30), 8551-5. DOI 10.1002/anie.201601546.
65. Famprikis, T.; Kudu, Ö. U.; Dawson, J. A.; Canepa, P.; Fauth, F.; Suard, E.; Zbiri, M.; Dambournet, D.; Borkiewicz, O. J.; Bouyanfif, H.; Emge, S. P.; Cretu, S.; Chotard, J.-N.; Grey, C. P.; Zeier, W. G.; Islam, M. S.; Masquelier, C., *Journal of the American Chemical Society* **2020,** *142* (43), 18422-18436. DOI 10.1021/jacs.0c06668.
66. de Klerk, N. J. J.; Wagemaker, M., *Chemistry of Materials* **2016,** *28* (9), 3122-3130. DOI 10.1021/acs.chemmater.6b00698.
67. Hayashi, A.; Noi, K.; Tanibata, N.; Nagao, M.; Tatsumisago, M., *Journal of Power Sources* **2014,** *258*, 420-423. DOI https://doi.org/10.1016/j.jpowsour.2014.02.054.
68. Yu, C.; Ganapathy, S.; de Klerk, N. J. J.; van Eck, E. R. H.; Wagemaker, M., *Journal of Materials Chemistry A* **2016,** *4* (39), 15095-15105. DOI 10.1039/C6TA05896E.
69. Nguyen, H.; Banerjee, A.; Wang, X.; Tan, D.; Wu, E. A.; Doux, J.-M.; Stephens, R.; Verbist, G.; Meng, Y. S., *Journal of Power Sources* **2019,** *435*, 126623. DOI https://doi.org/10.1016/j.jpowsour.2019.05.031.
70. Tsuji, F.; Nasu, A.; Sakuda, A.; Tatsumisago, M.; Hayashi, A., *Journal of Power Sources* **2021,** *506*, 230100. DOI https://doi.org/10.1016/j.jpowsour.2021.230100.
71. Tsuji, F.; Hoh, K. L.; Kim, K. H.; Sakuda, A.; Tatsumisago, M.; Martin, S. W.; Hayashi, A., *Journal of the Ceramic Society of Japan* **2021,** *129* (6), 323-328. DOI 10.2109/jcersj2.21010.
72. Yu, L.; Jiao, Q.; Liang, B.; Shan, H.; Lin, C.; Gao, C.; Shen, X.; Dai, S., *Journal of Alloys and Compounds* **2022,** *913*, 165229. DOI https://doi.org/10.1016/j.jallcom.2022.165229.
73. Shu, L.; Liang, B.; Yu, L.; Lin, C.; Gao, C.; Shen, X.; Liu, Y.; Jiao, Q., *Ceramics International* **2022,** *48* (23, Part A), 35134-35140. DOI https://doi.org/10.1016/j.ceramint.2022.08.109.
74. Tsuji, F.; Hoh, K.; Kim, K.; Sakuda, A.; Tatsumisago, M.; Martin, S.; Hayashi, A., *Journal of the Ceramic Society of Japan* **2021,** *129*, 323-328. DOI 10.2109/jcersj2.21010.
75. Wan, H.; Cai, L.; Weng, W.; Mwizerwa, J. P.; Yang, J.; Yao, X., *Journal of Power Sources* **2020,** *449*, 227515. DOI https://doi.org/10.1016/j.jpowsour.2019.227515.
76. Zhang, D.; Cao, X.; Xu, D.; Wang, N.; Yu, C.; Hu, W.; Yan, X.; Mi, J.; Wen, B.; Wang, L.; Zhang, L., *Electrochimica Acta* **2018,** *259*, 100-109. DOI 10.1016/j.electacta.2017.10.173.
77. Zhang, L.; Zhang, D.; Yang, K.; Yan, X.; Wang, L.; Mi, J.; Xu, B.; Li, Y., *Advanced Science* **2016,** *3* (10), 1600089. DOI https://doi.org/10.1002/advs.201600089.

78. Wang, N.; Yang, K.; Zhang, L.; Yan, X.; Wang, L.; Xu, B., *Journal of Materials Science* **2018,** *53* (3), 1987-1994. DOI 10.1007/s10853-017-1618-0.
79. Xiong, S.; Liu, Z.; Rong, H.; Wang, H.; McDaniel, M.; Chen, H., *Sci Rep-Uk* **2018,** *8* (1), 9146. DOI 10.1038/s41598-018-27301-8.
80. Heo, J. W.; Banerjee, A.; Park, K. H.; Jung, Y. S.; Hong, S.-T., *Advanced Energy Materials* **2018,** *8* (11), 1702716. DOI https://doi.org/10.1002/aenm.201702716.
81. Fuchs, T.; Culver, S. P.; Till, P.; Zeier, W. G., *ACS Energy Letters* **2020,** *5* (1), 146-151. DOI 10.1021/acsenergylett.9b02537.
82. Hibi, Y.; Tanibata, N.; Hayashi, A.; Tatsumisago, M., *Solid State Ionics* **2015,** *270*, 6-9. DOI https://doi.org/10.1016/j.ssi.2014.11.024.
83. Duchardt, M.; Ruschewitz, U.; Adams, S.; Dehnen, S.; Roling, B., *Angewandte Chemie International Edition* **2018,** *57* (5), 1351-1355. DOI https://doi.org/10.1002/anie.201712769.
84. Kraft, M. A.; Gronych, L. M.; Famprikis, T.; Ohno, S.; Zeier, W. G., *Chemistry of Materials* **2020,** *32* (15), 6566-6576. DOI 10.1021/acs.chemmater.0c01964.
85. Liu, Z.; Fu, W.; Payzant, E. A.; Yu, X.; Wu, Z.; Dudney, N. J.; Kiggans, J.; Hong, K.; Rondinone, A. J.; Liang, C., *Journal of the American Chemical Society* **2013,** *135* (3), 975-978. DOI 10.1021/ja3110895.
86. Lee, J. E.; Park, K.-H.; Kim, J. C.; Wi, T.-U.; Ha, A. R.; Song, Y. B.; Oh, D. Y.; Woo, J.; Kweon, S. H.; Yeom, S. J.; Cho, W.; Kim, K.; Lee, H.-W.; Kwak, S. K.; Jung, Y. S., *Advanced Materials* **2022,** *34* (16), 2200083. DOI https://doi.org/10.1002/adma.202200083.
87. Wang, H.; Hood, Z. D.; Xia, Y.; Liang, C., *Journal of Materials Chemistry A* **2016,** *4* (21), 8091-8096. DOI 10.1039/c6ta02294d.
88. Uematsu, M.; Yubuchi, S.; Tsuji, F.; Sakuda, A.; Hayashi, A.; Tatsumisago, M., *Journal of Power Sources* **2019,** *428*, 131-135. DOI https://doi.org/10.1016/j.jpowsour.2019.04.069.
89. Yubuchi, S.; Hayashi, A.; Tatsumisago, M., *Chemistry Letters* **2015,** *44* (7), 884-886. DOI 10.1246/cl.150195.
90. Uematsu, M.; Yubuchi, S.; Noi, K.; Sakuda, A.; Hayashi, A.; Tatsumisago, M., *Solid State Ionics* **2018,** *320*, 33-37. DOI https://doi.org/10.1016/j.ssi.2017.12.021.
91. Vaselabadi, S. A.; Smith, W. H.; Wolden, C. A., *Journal of The Electrochemical Society* **2021,** *168* (11), 110533. DOI 10.1149/1945-7111/ac3752.
92. Guo, Y.; Shi, X.; Ma, Y.; Song, D.; Zhang, H.; Li, C.; Zhang, L., *Batteries & Supercaps* **2023,** *6* (1), e202200353. DOI https://doi.org/10.1002/batt.202200353.
93. Wan, H.; Mwizerwa, J. P.; Han, F.; Weng, W.; Yang, J.; Wang, C.; Yao, X., *Nano Energy* **2019,** *66*, 104109. DOI https://doi.org/10.1016/j.nanoen.2019.104109.
94. Zhang, X.; Phuah, K. C.; Adams, S., *Chemistry of Materials* **2021,** *33* (23), 9184-9193. DOI 10.1021/acs.chemmater.1c02712.
95. Nakajima, H.; Tsukasaki, H.; Ding, J.; Kimura, T.; Nakano, T.; Nasu, A.; Hirata, A.; Sakuda, A.; Hayashi, A.; Mori, S., *Journal of Power Sources* **2021,** *511*, 230444. DOI https://doi.org/10.1016/j.jpowsour.2021.230444.
96. Hayashi, A.; Noi, K.; Tanibata, N.; Nagao, M.; Tatsumisago, M., *J. Power Sources* **2014,** *258*, 420-423. DOI 10.1016/j.jpowsour.2014.02.054.
97. Krauskopf, T.; Muy, S.; Culver, S. P.; Ohno, S.; Delaire, O.; Shao-Horn, Y.; Zeier, W. G., *Journal of the American Chemical Society* **2018,** *140* (43), 14464-14473. DOI 10.1021/jacs.8b09340.
98. Krauskopf, T.; Culver, S. P.; Zeier, W. G., *Inorganic Chemistry* **2018,** *57* (8), 4739-4744. DOI 10.1021/acs.inorgchem.8b00458.
99. Famprikis, T.; Bouyanfif, H.; Canepa, P.; Zbiri, M.; Dawson, J. A.; Suard, E.; Fauth, F.; Playford, H. Y.; Dambournet, D.; Borkiewicz, O. J.; Courty, M.; Clemens, O.; Chotard, J.-N.; Islam, M. S.; Masquelier, C., *Chemistry of Materials* **2021,** *33* (14), 5652-5667. DOI 10.1021/acs.chemmater.1c01113.

100. Famprikis, T.; Dawson, J. A.; Fauth, F.; Clemens, O.; Suard, E.; Fleutot, B.; Courty, M.; Chotard, J.-N.; Islam, M. S.; Masquelier, C., *ACS Materials Letters* **2019,** *1* (6), 641-646. DOI 10.1021/acsmaterialslett.9b00322.
101. Yang, L.; Geng, S.; He, Y.; Ming, X.; Kuang, X., *The Journal of Physical Chemistry C* **2022,** *126* (14), 6161-6170. DOI 10.1021/acs.jpcc.2c00850.
102. Gupta, M. K.; Ding, J.; Osti, N. C.; Abernathy, D. L.; Arnold, W.; Wang, H.; Hood, Z.; Delaire, O., *Energy & Environmental Science* **2021,** *14* (12), 6554-6563. DOI 10.1039/D1EE01509E.
103. Tanibata, N.; Noi, K.; Hayashi, A.; Tatsumisago, M., *RSC Advances* **2014,** *4* (33), 17120-17123. DOI 10.1039/C4RA00996G.
104. Zhu, Z.; Chu, I.-H.; Deng, Z.; Ong, S. P., *Chemistry of Materials* **2015,** *27* (24), 8318-8325. DOI 10.1021/acs.chemmater.5b03656.
105. Rao, R. P.; Chen, H.; Wong, L. L.; Adams, S., *Journal of Materials Chemistry A* **2017,** *5* (7), 3377-3388. DOI 10.1039/C6TA09809F.
106. Yu, Z.; Shang, S.-L.; Seo, J.-H.; Wang, D.; Luo, X.; Huang, Q.; Chen, S.; Lu, J.; Li, X.; Liu, Z.-K.; Wang, D., *Advanced Materials* **2017,** *29* (16), 1605561. DOI https://doi.org/10.1002/adma.201605561.
107. Huang, B.; Zhang, J.; Shi, Y.; Lu, X.; Zhang, J.; Chen, B.; Zhou, J.; Cai, R., *Physical Chemistry Chemical Physics* **2020,** *22* (35), 19816-19822. DOI 10.1039/D0CP03487H.
108. He, R.; Hu, Z.; Gao, J.; Zhang, G.; Shen, K., *The Journal of Physical Chemistry C* **2022,** *126* (25), 10593-10600. DOI 10.1021/acs.jpcc.2c02847.
109. Chu, I.-H.; Kompella, C. S.; Nguyen, H.; Zhu, Z.; Hy, S.; Deng, Z.; Meng, Y. S.; Ong, S. P., *Scientific Reports* **2016,** *6* (1), 33733. DOI 10.1038/srep33733.
110. Huang, H.; Wu, H.-H.; Wang, X.; Huang, B.; Zhang, T.-Y., *Physical Chemistry Chemical Physics* **2018,** *20* (31), 20525-20533. DOI 10.1039/C8CP02383B.
111. Bo, S.-H.; Wang, Y.; Kim, J. C.; Richards, W. D.; Ceder, G., *Chemistry of Materials* **2016,** *28* (1), 252-258. DOI 10.1021/acs.chemmater.5b04013.
112. Wang, H.; Yu, M.; Wang, Y.; Feng, Z.; Wang, Y.; Lü, X.; Zhu, J.; Ren, Y.; Liang, C., *Journal of Power Sources* **2018,** *401*, 111-116. DOI https://doi.org/10.1016/j.jpowsour.2018.05.037.
113. Halacoglu, S.; Chertmanova, S.; Chen, Y.; Li, Y.; Rajapakse, M.; Sumanasekera, G.; Narayanan, B.; Wang, H., *ChemSusChem* **2021,** *14* (23), 5161-5166. DOI https://doi.org/10.1002/cssc.202101839.
114. Wang, H.; Chen, Y.; Hood, Z. D.; Keum, J. K.; Pandian, A. S.; Chi, M.; An, K.; Liang, C.; Sunkara, M. K., *ACS Applied Energy Materials* **2018,** *1* (12), 7028-7034. DOI 10.1021/acsaem.8b01449.
115. Zhang, L.; Zhang, D.; Yang, K.; Yan, X.; Wang, L.; Mi, J.; Xu, B.; Li, Y., *Adv. Sci.* **2016,** *3* (10), 1600089. DOI 10.1002/advs.201600089.
116. Gamo, H.; Phuc, N. H. H.; Matsuda, R.; Muto, H.; Matsuda, A., *Materials Today Energy* **2019,** *13*, 45-49. DOI https://doi.org/10.1016/j.mtener.2019.04.012.
117. Zhang, Q.; Zhang, C.; Hood, Z. D.; Chi, M.; Liang, C.; Jalarvo, N. H.; Yu, M.; Wang, H., *Chemistry of Materials* **2020,** *32* (6), 2264-2271. DOI 10.1021/acs.chemmater.9b03879.
118. Jalem, R.; Hayashi, A.; Tsuji, F.; Sakuda, A.; Tateyama, Y., *Chemistry of Materials* **2020,** *32* (19), 8373-8381. DOI 10.1021/acs.chemmater.0c02318.
119. Seo, J. Y.; Shim, S.; Lee, J.-W.; Lee, B. D.; Park, S.; Park, W. B.; Han, S.; Pyo, M.; Sohn, K.-S., *Journal of Materials Chemistry A* **2022,** *10* (4), 1831-1839. DOI 10.1039/D1TA09886A.
120. Cao, H.; Yu, M.; Zhang, L.; Zhang, Z.; Yan, X.; Li, P.; Yu, C., *Journal of Materials Science & Technology* **2021,** *70*, 168-175. DOI https://doi.org/10.1016/j.jmst.2020.08.035.
121. Feng, X.; Fang, H.; Liu, P.; Wu, N.; Self, E. C.; Yin, L.; Wang, P.; Li, X.; Jena, P.; Nanda, J., *Angewandte Chemie* **2021,** *133* (50), 26362-26370.

122. Kandagal, V. S.; Bharadwaj, M. D.; Waghmare, U. V., *Journal of Materials Chemistry A* **2015,** *3* (24), 12992-12999. DOI 10.1039/C5TA01616A.
123. Ong, S. P.; Mo, Y.; Richards, W. D.; Miara, L.; Lee, H. S.; Ceder, G., *Energy & Environmental Science* **2013,** *6* (1), 148-156. DOI 10.1039/C2EE23355J.
124. Richards, W. D.; Tsujimura, T.; Miara, L. J.; Wang, Y.; Kim, J. C.; Ong, S. P.; Uechi, I.; Suzuki, N.; Ceder, G., *Nature Communications* **2016,** *7* (1), 11009. DOI 10.1038/ncomms11009.
125. Duchardt, M.; Neuberger, S.; Ruschewitz, U.; Krauskopf, T.; Zeier, W. G.; Schmedt auf der Günne, J.; Adams, S.; Roling, B.; Dehnen, S., *Chemistry of Materials* **2018,** *30* (12), 4134-4139. DOI 10.1021/acs.chemmater.8b01656.
126. Zhang, Z.; Roy, P.-N.; Li, H.; Avdeev, M.; Nazar, L. F., *Journal of the American Chemical Society* **2019,** *141* (49), 19360-19372. DOI 10.1021/jacs.9b09343.
127. Ramos, E. P.; Zhang, Z.; Assoud, A.; Kaup, K.; Lalère, F.; Nazar, L. F., *Chemistry of Materials* **2018,** *30* (21), 7413-7417. DOI 10.1021/acs.chemmater.8b02077.
128. Benedek, P.; Yazdani, N.; Chen, H.; Wenzler, N.; Juranyi, F.; Månsson, M.; Islam, M. S.; Wood, V. C., *Sustainable Energy & Fuels* **2019,** *3* (2), 508-513. DOI 10.1039/C8SE00389K.
129. Kraft, M. A.; Gronych, L. M.; Famprikis, T.; Zeier, W. G., *ACS Applied Energy Materials* **2021,** *4* (7), 7250-7258. DOI 10.1021/acsaem.1c01367.
130. Zhu, Z.; Tang, H.; Qi, J.; Li, X.-G.; Ong, S. P., *Advanced Energy Materials* **2021,** *11* (7), 2003196. DOI https://doi.org/10.1002/aenm.202003196.
131. Tian, Y.; Shi, T.; Richards, W. D.; Li, J.; Kim, J. C.; Bo, S.-H.; Ceder, G., *Energy & Environmental Science* **2017,** *10* (5), 1150-1166. DOI 10.1039/c7ee00534b.
132. Zhu, Y.; He, X.; Mo, Y., *ACS Appl Mater Interfaces* **2015,** *7* (42), 23685-93. DOI 10.1021/acsami.5b07517.
133. Han, F.; Zhu, Y.; He, X.; Mo, Y.; Wang, C., *Advanced Energy Materials* **2016,** *6* (8), 1501590. DOI https://doi.org/10.1002/aenm.201501590.
134. Zhu, Y.; He, X.; Mo, Y., *Journal of Materials Chemistry A* **2016,** *4* (9), 3253-3266. DOI 10.1039/c5ta08574h.
135. Deysher, G.; Chen, Y.-T.; Sayahpour, B.; Lin, S. W.-H.; Ham, S.-Y.; Ridley, P.; Cronk, A.; Wu, E. A.; Tan, D. H. S.; Doux, J.-M.; Oh, J. A. S.; Jang, J.; Nguyen, L. H. B.; Meng, Y. S., *ACS Applied Materials & Interfaces* **2022,** *14* (42), 47706-47715. DOI 10.1021/acsami.2c12759.
136. An, T.; Jia, H.; Peng, L.; Xie, J., *ACS Applied Materials & Interfaces* **2020,** *12* (18), 20563-20569. DOI 10.1021/acsami.0c03899.
137. Chu, I. H.; Kompella, C. S.; Nguyen, H.; Zhu, Z.; Hy, S.; Deng, Z.; Meng, Y. S.; Ong, S. P., *Sci Rep* **2016,** *6*, 33733. DOI 10.1038/srep33733.
138. Wu, E. A.; Kompella, C. S.; Zhu, Z.; Lee, J. Z.; Lee, S. C.; Chu, I.-H.; Nguyen, H.; Ong, S. P.; Banerjee, A.; Meng, Y. S., *ACS Applied Materials & Interfaces* **2018,** *10* (12), 10076-10086. DOI 10.1021/acsami.7b19037.
139. Lazar, M.; Kmiec, S.; Joyce, A.; Martin, S. W., *ACS Applied Energy Materials* **2020,** *3* (12), 11559-11569. DOI 10.1021/acsaem.0c00914.
140. Hänsel, C.; Kumar, P. V.; Kundu, D., *Chemistry of Materials* **2020,** *32* (24), 10501-10510. DOI 10.1021/acs.chemmater.0c03444.
141. Li, L.; Xu, R.; Zhang, L.; Zhang, Z.; Yang, M.; Liu, D.; Yan, X.; Zhou, A., *Advanced Functional Materials* **2022,** *32* (31), 2203095. DOI https://doi.org/10.1002/adfm.202203095.
142. Tian, Y.; Sun, Y.; Hannah, D. C.; Xiao, Y.; Liu, H.; Chapman, K. W.; Bo, S.-H.; Ceder, G., *Joule* **2019,** *3* (4), 1037-1050. DOI https://doi.org/10.1016/j.joule.2018.12.019.
143. Zhang, S.; Zhao, Y.; Zhao, F.; Zhang, L.; Wang, C.; Li, X.; Liang, J.; Li, W.; Sun, Q.; Yu, C.; Luo, J.; Doyle-Davis, K.; Li, R.; Sham, T.-K.; Sun, X., *Advanced Functional Materials* **2020,** *30* (22), 2001118. DOI https://doi.org/10.1002/adfm.202001118.

144. Zhao, Y.; Liang, J.; Sun, Q.; Goncharova, Lyudmila V.; Wang, J.; Wang, C.; Adair, K. R.; Li, X.; Zhao, F.; Sun, Y.; Li, R.; Sun, X., *Journal of Materials Chemistry A* **2019,** *7* (8), 4119-4125. DOI 10.1039/C8TA10174D.
145. Hu, P.; Zhang, Y.; Chi, X.; Kumar Rao, K.; Hao, F.; Dong, H.; Guo, F.; Ren, Y.; Grabow, L. C.; Yao, Y., *ACS Applied Materials & Interfaces* **2019,** *11* (10), 9672-9678. DOI 10.1021/acsami.8b19984.
146. Li, Y.; Halacoglu, S.; Shreyas, V.; Arnold, W.; Guo, X.; Dou, Q.; Jasinski, J. B.; Narayanan, B.; Wang, H., *Chemical Engineering Journal* **2022,** *434*, 134679. DOI https://doi.org/10.1016/j.cej.2022.134679.
147. Li, Y.; Arnold, W.; Halacoglu, S.; Jasinski, J. B.; Druffel, T.; Wang, H., *Advanced Functional Materials* **2021,** *31* (28), 2101636. DOI https://doi.org/10.1002/adfm.202101636.
148. Yue, J.; Zhu, X.; Han, F.; Fan, X.; Wang, L.; Yang, J.; Wang, C., *ACS Applied Materials & Interfaces* **2018,** *10* (46), 39645-39650. DOI 10.1021/acsami.8b12610.
149. Ge, P.; Zhang, L.; Zhao, W.; Yang, Y.; Sun, W.; Ji, X., *Advanced Functional Materials* **2020,** *30* (16), 1910599. DOI https://doi.org/10.1002/adfm.201910599.
150. Zhao, W.; Zhang, L.; Jiang, F.; Chang, X.; Yang, Y.; Ge, P.; Sun, W.; Ji, X., *Journal of Materials Chemistry A* **2020,** *8* (10), 5284-5297. DOI 10.1039/C9TA13899D.
151. Santhosha, A. L.; Medenbach, L.; Palaniselvam, T.; Adelhelm, P., *The Journal of Physical Chemistry C* **2020,** *124* (19), 10298-10305. DOI 10.1021/acs.jpcc.0c00387.
152. Wan, H.; Mwizerwa, J. P.; Qi, X.; Liu, X.; Xu, X.; Li, H.; Hu, Y.-S.; Yao, X., *ACS Nano* **2018,** *12* (3), 2809-2817. DOI 10.1021/acsnano.8b00073.
153. Shirota, G.; Nasu, A.; Deguchi, M.; Sakuda, A.; Tatsumisago, M.; Hayashi, A., *Journal of the Ceramic Society of Japan* **2022,** *130* (4), 308-312. DOI 10.2109/jcersj2.21177.
154. Tanibata, N.; Matsuyama, T.; Hayashi, A.; Tatsumisago, M., *Journal of Power Sources* **2015,** *275*, 284-287. DOI https://doi.org/10.1016/j.jpowsour.2014.10.193.
155. Yuan, S.; Zhao, W.; Zeng, Z.; Dong, Y.; Yang, Y.; Sun, W.; Ge, P., *Journal of Materials Chemistry A* **2022,** *10* (10), 5488-5504. DOI 10.1039/D1TA10832H.
156. Zhao, W.; Yuan, S.; Lei, S.; Zeng, Z.; Dong, J.; Jiang, F.; Yang, Y.; Sun, W.; Ji, X.; Ge, P., *Advanced Functional Materials* **2023,** *33* (5), 2211542. DOI https://doi.org/10.1002/adfm.202211542.
157. Zhang, Z.; Cao, H.; Yang, M.; Yan, X.; Yu, C.; Liu, D.; Zhang, L., *Journal of Energy Chemistry* **2020,** *48*, 250-258. DOI https://doi.org/10.1016/j.jechem.2020.01.014.
158. Yue, J.; Han, F.; Fan, X.; Zhu, X.; Ma, Z.; Yang, J.; Wang, C., *ACS Nano* **2017,** *11* (5), 4885-4891. DOI 10.1021/acsnano.7b01445.
159. Fan, X.; Yue, J.; Han, F.; Chen, J.; Deng, T.; Zhou, X.; Hou, S.; Wang, C., *ACS Nano* **2018,** *12* (4), 3360-3368. DOI 10.1021/acsnano.7b08856.
160. Tanibata, N.; Deguchi, M.; Hayashi, A.; Tatsumisago, M., *Chemistry of Materials* **2017,** *29* (12), 5232-5238. DOI 10.1021/acs.chemmater.7b01116.
161. Tanibata, N.; Tsukasaki, H.; Deguchi, M.; Mori, S.; Hayashi, A.; Tatsumisago, M., *Solid State Ionics* **2017,** *311*, 6-13. DOI https://doi.org/10.1016/j.ssi.2017.08.022.
162. Wan, H.; Weng, W.; Han, F.; Cai, L.; Wang, C.; Yao, X., *Nano Today* **2020,** *33*, 100860. DOI https://doi.org/10.1016/j.nantod.2020.100860.
163. Ando, T.; Sakuda, A.; Tatsumisago, M.; Hayashi, A., *Electrochem Commun* **2020,** *116*, 106741. DOI https://doi.org/10.1016/j.elecom.2020.106741.
164. Tang, H.; Deng, Z.; Lin, Z.; Wang, Z.; Chu, I.-H.; Chen, C.; Zhu, Z.; Zheng, C.; Ong, S. P., *Chemistry of Materials* **2018,** *30* (1), 163-173. DOI 10.1021/acs.chemmater.7b04096.
165. Nagata, Y.; Nagao, K.; Deguchi, M.; Sakuda, A.; Hayashi, A.; Tsukasaki, H.; Mori, S.; Tatsumisago, M., *Chemistry of Materials* **2018,** *30* (20), 6998-7004. DOI 10.1021/acs.chemmater.8b01872.

166. Chi, X.; Liang, Y.; Hao, F.; Zhang, Y.; Whiteley, J.; Dong, H.; Hu, P.; Lee, S.; Yao, Y., *Angewandte Chemie International Edition* **2018,** *57* (10), 2630-2634. DOI https://doi.org/10.1002/anie.201712895.
167. Hao, F.; Chi, X.; Liang, Y.; Zhang, Y.; Xu, R.; Guo, H.; Terlier, T.; Dong, H.; Zhao, K.; Lou, J.; Yao, Y., *Joule* **2019,** *3* (5), 1349-1359. DOI https://doi.org/10.1016/j.joule.2019.03.017.
168. Banerjee, A.; Park, K. H.; Heo, J. W.; Nam, Y. J.; Moon, C. K.; Oh, S. M.; Hong, S. T.; Jung, Y. S., *Angewandte Chemie* **2016,** *128* (33), 9786-9790.

Authors Biographies

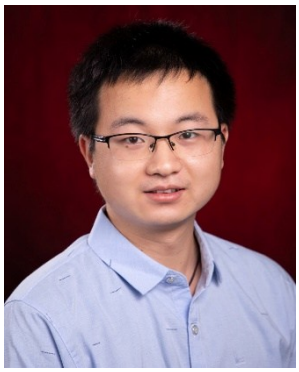

Xiaolin Guo is currently a Ph.D. candidate of Mechanical Engineering, under the supervision of Prof. Hui Wang at University of Louisville. He received his master's degree in the major of Materials Science from the Huazhong University of Science and Technology in 2018. His research interests focus on synthesis of solid-state ion conductors, solid-state batteries and interface modifications.

Selim Halacoglu received his bachelor's degree in the major of Automotive Engineering in 2013 from Cukurova University, Turkiye and received his master's degree in the major of Automotive Engineering in 2018 from the University of Hertfordshire, United Kingdom. He is currently a Ph.D. candidate under the supervision of Prof. Hui Wang at the University of Louisville, Kentucky. His current studies focus on the synthesis and development of solid-state electrolytes and solid-state batteries.

Yan Chen is a neutron scattering scientist at the VULCAN diffractometer at the Spallation Neutron Source at Oak Ridge National Laboratory. He received his PhD degree in materials science from the University of Central Florida. His research interests include synthesis mechanism, structural transition and deformation behavior in compounds, alloys, and heterogeneous materials for energy and engineering applications via *in situ* neutron diffraction. Chen can be reached by email at cheny1@ornl.gov.

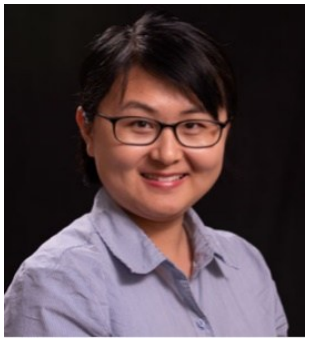

Hui Wang is an Associate professor of Mechanical Engineering at University of Louisville, Kentucky. She received her PhD degree in Materials Science and Engineering from Michigan Tech University, and then work as a postdoctoral researcher at the Oak Ridge National Laboratory. Her research interests include advanced materials for energy conversion and storage, such as lithium/sodium ion conductors, carbon and 2D materials for photovoltaics. Recently, her group research focus on synthesis and interface studies for rechargeable alkaline metal batteries. She is the recipient of 2021 NSF Career Award and 2020 NSF EPSCoR Research Fellow and is recognized as UofL Emerging Researcher of the year 2022. Wang can be reached by email at hui.wang.1@louisville.edu.